

1 **Buoyant calving and ice-contact lake evolution at Pasterze Glacier (Austria) in the period**
2 **1998-2019**

3

4

5 Andreas Kellerer-Pirklbauer (1), Michael Avian (2), Douglas I. Benn (3), Felix Bernsteiner (1),

6 Philipp Krisch (1), Christian Ziesler (1)

7

8 (1) Cascade - The mountain processes and mountain hazards group, Institute of Geography and

9 Regional Science, University of Graz, Austria

10 (2) Department of Earth Observation, Zentralanstalt für Meteorologie und Geodynamik

11 (ZAMG), Vienna, Austria

12 (3) School of Geography and Geosciences, University of St Andrews, St Andrews, UK

13

14 **Correspondence**

15 Andreas Kellerer-Pirklbauer; andreas.kellerer@uni-graz.at

16

17 **Funding information**

18 Research relevant for this study was funded through different projects: (a)

19 Austrian Science Fund, project no. FWF P18304-N10, (b) Hohe Tauern National Park authority

20 (various projects), (c) Glockner Ökofonds (GROHAG) 2018, and (d) Austrian Alpine Association

21 (through the annual glacier monitoring program)

22

23 **Abstract:** Rapid growth of proglacial lakes in the current warming climate can pose significant
24 outburst flood hazards, increase rates of ice mass loss, and alter the dynamic state of glaciers.
25 We studied the nature and rate of proglacial lake evolution at Pasterze Glacier (Austria) in the
26 period 1998-2019 using different remote sensing (photogrammetry, laserscanning) and
27 fieldwork-based (~~GPS~~GNSS, time-lapse photography, geoelectrical resistivity tomography/ERT,
28 and bathymetry) data. Glacier thinning below the spillway level and glacier recession caused
29 flooding of the glacier, initially forming a glacier-lateral to supraglacial lake with subaerial and
30 subaquatic debris-covered dead-ice bodies. The observed lake size increase in 1998-2019
31 followed an exponential curve (1998: 1900 m²; 2019: 304,000 m²). ERT data from 2015 to 2019
32 revealed widespread existence of massive dead-ice bodies exceeding 25 m in thickness near the
33 lake shore. Several large-scale and rapidly occurring buoyant calving events were detected in
34 the 48 m deep basin by time-lapse photography, indicating that buoyant calving is a crucial
35 process for the fast lake expansion. [Estimations of the ice volume losses by buoyant calving and](#)
36 [by subaerial ablation at a 0.35 km² large lake-proximal section of the glacier reveal comparable](#)
37 [values for both processes \(c.1 x 10⁶ m³\) for the period August 2018 to August 2019.](#) We
38 identified a sequence of processes: glacier recession into a basin and glacier thinning below
39 spillway-level; glacio-fluvial sedimentation in the glacial-proglacial transition zone covering
40 dead ice; initial formation and accelerating enlargement of a glacier-lateral to supraglacial lake
41 by ablation of glacier ice and debris-covered dead ice forming thermokarst features; increase in
42 hydrostatic disequilibrium leading to destabilization of ice at the lake bottom or at the near-
43 shore causing fracturing, tilting, disintegration or emergence of new icebergs due to buoyant
44 calving; and gradual melting of icebergs along with iceberg capsizing events. We conclude that

45 buoyant calving, previously not reported from the European Alps, might play an important role
46 at alpine glaciers in the future as many glaciers are expected to recede into valley or cirque
47 overdeepenings.

48

49 **Keywords:** ice-contact lake; dead ice decay; buoyant calving; hydrostatic equilibrium; proglacial
50 landscape evolution

51

52 **1. INTRODUCTION**

53 Ongoing recession of mountain glaciers worldwide reveals dynamic landscapes exposed to high
54 rates of geomorphological and hydrological changes (Carrivick and Heckmann, 2017). In suitable
55 topographic conditions, proglacial lakes may form, including ice-contact lakes (physically
56 attached to an ice margin) and ice-marginal lakes (lakes detached from or immediately beyond
57 a contemporary ice margin) (Benn and Evans, 2010; Carrivick and Tweed, 2013). Such lakes
58 have increased in number, size and volume around the world due to climate warming-induced
59 glacier melt (Carrivick and Tweed, 2013; Otto, 2019). Buckel et al. (2018) for instance studied
60 the formation and distribution of proglacial lakes since the Little Ice Age (LIA) in Austria
61 revealing a continuous acceleration in the number of glacier-related lakes particularly since the
62 turn of the 21st century.

63

64 The formation of proglacial lakes is important because they can pose significant outburst flood
65 hazards (e.g. Richardson and Reynolds, 2000; Harrison et al., 2018), increase rates of ice mass
66 loss, and alter the dynamic state of glaciers (e.g. Kirkbride and Warren, 1999; King et al., 2018,

67 2019; Liu et al., 2020). However, detailed descriptions of proglacial lake formation and related
68 subaerial and subaquatic processes are still rare. Carrivick and Heckmann (2017) pointed out
69 that there is an urgent need for inventories of proglacial systems including lakes to form a
70 baseline from which changes could be detected.

71

72 The evolution of proglacial lakes is commonly linked to the subsurface, particularly to changes
73 in the distribution of debris-covered dead ice (defined here as any part of a glacier which has
74 ceased to flow) and permafrost-related ground ice bodies (Bosson et al., 2015; Gärtner-Roer
75 and Bast, 2019) affecting lake geometry and areal expansion.

76

77 Water bodies at the glacier surface form initially as supraglacial lakes which might be either
78 perched lakes (i.e. above the hydrological base level of the glacier) or base-level lakes (spillway
79 controlled). The former type is prone to drainage if the perched lake connects to the englacial
80 conduit system (Benn et al., 2001). Rapid areal expansion of such lakes is controlled by
81 waterline and subaerial melting of exposed ice cliffs and calving (Benn et al., 2001).

82 Furthermore, supraglacial lakes may transform into proglacial lakes lacking any ice core (full-
83 depth lakes) through melting of lake-bottom ice. However, this is a slow process in which
84 energy is conducted from the overlying water and cannot account for some observed instances
85 of fast lake-bottom lowering with rates exceeding $\approx 10 \text{ m yr}^{-1}$ (Thompson et al., 2012). It has
86 been argued that fast lake-bottom lowering could occur by buoyant calving (Dykes et al., 2010;
87 Thompson et al., 2012), but the rare and episodic nature of such events mean that little is

88 known about how buoyant calving might contribute to the transformation of supraglacial lakes
89 into full-depth lakes.

90

91 ~~Ablation of lake-terminating glaciers may lead to the development of submerged ice feet or~~
92 ~~thinning of ice margins below the point of hydrostatic equilibrium. Rises in lake level can have~~
93 ~~similar results. In such cases, ice becomes super-buoyant and subject to net upward buoyant~~
94 ~~forces, promoting fracture propagation and calving (Benn et al., 2007). Calving by this process~~
95 ~~has been described by Holdsworth (1973), Warren et al. (2001) and Boyce et al. (2007). Buoyant~~
96 ~~calving occurs where ice is subject to net upward buoyant forces sufficient to overcome its~~
97 ~~tensile strength. Such forces can develop where either ice thinning (e.g. via surface ablation) or~~
98 ~~water deepening (e.g. rises in lake level) cause the ice to become buoyant. If the ice is unable to~~
99 ~~adjust its geometry to achieve hydrostatic equilibrium it can become super-buoyant (Benn et~~
100 ~~al., 2007), creating tensile stresses at the ice base. If these stresses become sufficiently high,~~
101 ~~the ice will fracture and calve, as described by Holdsworth (1973), Warren et al. (2001) and~~
102 ~~Boyce et al. (2007). Detailed models of super-buoyancy and buoyant calving have been~~
103 ~~presented by Wagner et al. (2016) and Benn et al. (2017).~~ Hydrostatic disequilibrium caused the
104 sudden disintegration of debris-covered dead ice in the proglacial area of Pasterze Glacier in
105 September 2016 (Fig. 2). This event was briefly described in Kellerer-Pirklbauer et al. (2017) and
106 was one of the main motivations for the present study.

107

108 In ~~the present~~this study, we analysed rates and processes of glacier recession and formation
109 and evolution of an ice-contact lake at Pasterze Glacier, Austria, over a period of 22 years. The

110 aims of this study are (i) to examine glaciological and morphological changes at the highly
111 dynamic glacial-proglacial transition zone of the receding Pasterze Glacier and (ii) to discuss
112 related processes which formed the proglacial lake named Pasterzensee (See is German for
113 lake) during the period 1998-2019. Regarding the latter, we focus particularly on the
114 significance of buoyant calving. In doing so, we consider subaerial, subsurface, aquatic, as well
115 as subaquatic domains applying fieldwork-based and remote-sensing techniques.

116

117 **2. STUDY AREA**

118 The study area comprises the glacial-proglacial transition zone of Pasterze Glacier, Austria. This
119 glacier covered 26.5 km² during the LIA maximum around 1850 and is ~~currently~~ the largest
120 glacier in the Austrian Alps with an area of 15.4 km² in 2019 (Fig. 1). The glacier is located in the
121 Glockner Mountains, Hohe Tauern Range, at 47°05'N and 12°43'E (Fig. 1b). The gently sloping,
122 4.5 km long glacier tongue is connected to the upper part of the glacier by an icefall named
123 Hufeisenbruch (meaning “horseshoe icefall” in German) attributed to its former shape in plan
124 view. This icefall disintegrated and narrowed substantially during the last decades attributed to
125 the decrease of ice replenishment from the upper to the lower part of the glacier (Kellerer-
126 Pirklbauer, et al. 2008; Kaufmann et al., 2015).

127

128 The longest time series of length changes at Austrian glaciers has been compiled for Pasterze
129 Glacier. Measurements at this glacier were initiated in 1879 and interrupted in only three years.
130 Furthermore, annual glacier flow velocity measurements and surface elevation changes at
131 cross-sections were initiated in the 1920s with almost continuous measurements since then

132 [\(Lieb and Kellerer-Pirklbauer, 2018, chapter 4.2.\)](#)~~(Wakonigg and Lieb, 1996)~~. Technical details of
133 the measurement can be found in Kellerer-Pirklbauer et al. (2008) ~~as well as in~~ [and](#) Lieb and
134 Kellerer-Pirklbauer (2018). Minor glacier advances at Pasterze Glacier occurred in only seven
135 years since 1879, the most recent of which was in the 1930s. Even during wetter and cooler
136 periods (1890s, 1920s and 1965-1980), the glacier did not advance substantially, which can be
137 attributed to the long response time of the glacier (Zuo and Oerlemans, 1997). In 1959-2019,
138 Pasterze Glacier receded by 1550 m, three times the mean value for all Austrian glaciers (520
139 m), related to its large size. Today, Pasterze Glacier is characterised by annual mean recession
140 rates in the order of 40 m yr^{-1} (Lieb and Kellerer-Pirklbauer, 2018) causing a rather high pace of
141 glacial to proglacial landscape modification favouring paraglacial response processes
142 (Ballantyne, 2002; Avian et al., 2018).

143
144 Analyses of brittle and ductile structures at the surface of the glacier tongue revealed that
145 many of these structures are relict and independent from current glacier motion (Kellerer-
146 Pirklbauer and Kulmer, 2019). The glacier tongue is in a state of rapid decay and thinning and
147 thus prone to fracturing by normal fault formation. Englacial and subglacial melting of glacier
148 ice caused the formation of circular collapse structures with concentric crevasses, which form
149 when the ice between the glacier surface and the roof of water channels decreases. Kellerer-
150 Pirklbauer and Kulmer (2019) concluded that the tongue of the Pasterze Glacier is currently
151 turning into a large dead-ice body characterized by a strong decrease in ice replenishment from
152 further up-glacier, movement cessation, accelerated thinning and ice disintegration by supra-,
153 en- and subglacial ablation, allowing normal fractures and circular collapse features to develop.

154 This rapid deglaciation and decrease in activity are favourable for dead ice and proglacial lake
155 formation.

156
157 An automatic weather station is located close to the study area operated by Austrian Hydro
158 Powers since 1982 (AWS in Fig. 1a). The coldest calendar year in the period 1998-2019 was
159 2005 with a mean annual air temperature (MAAT) of 0.9°C whereas the warmest year was 2015
160 with 4.0°C (range 3.1°C, mean of the 22-year period 2.4°C; Fig. 1c). Interannual variation is high
161 although a warming trend is clear. A MAAT value >3°C was calculated for eight of the nine years
162 between 2011 and 2019. No such high MAAT values were recorded for the entire previous 28-
163 year period 1982-2010 indicating significant recent atmospheric warming. Two ground
164 temperature monitoring sites were installed near the lake in fluvio-glacial sediments in 2018
165 (PRO1 – one sensor at the surface; PRO2 – three sensors at the surface and at 10 and 40 cm
166 depths; location see Fig. 1a) using GeoPrecision data logger equipped with PT1000 temperature
167 sensors (accuracy of +/-0.05°C) and logging hourly. Positive mean values for a 363-day long
168 period (13.09.2018-10.09.2019) were recorded for both sites (PRO1: 2.6°C, PRO2: 3.7-3.9°C)
169 suggesting permafrost-free conditions in the proglacial area and unfavourable conditions for
170 long-term dead ice conservation even below a protecting sediment cover.

171

172 **3. MATERIAL AND METHODS**

173 **3.1. GNSS data**

174 The terminus position of Pasterze Glacier was measured directly in the field by Global
175 Navigation Satellite System (GNSS) techniques in 14 years between 2003 and 2019 (annually

176 between 2003 and 2005, in 2008, and annually between 2010 and 2019). Direct measurements
177 of the subaerial glacier limit are essential in areas where debris cover obscures the glacier
178 margin, hindering the successful application of remote-sensing techniques (e.g. Kaufmann et
179 al., 2015; Avian et al., 2020). GNSS measurements were mostly carried out in September of the
180 above listed years, thus, close to the end of the glaciological years of mid-latitude mountain
181 regions. Until 2013, conventional ~~GPS~~-GNSS technique was applied using different handheld
182 GARMIN devices (geometric accuracy in the range of meters). Afterwards, real time kinematics
183 (RTK) technique was used, where correction data from the base station whose location is
184 precisely known are transmitted to the rover (geometric accuracy in the range of centimetres).
185 We utilized a TOPCON HiPer V Differential GPS-~~(DGPS)~~ system. The base station was either our
186 own local station (base-and-rover setup) or we obtained correction signals from a national
187 correction-data provider (EPOSA, Vienna).

188

189 **3.2. Airborne photogrammetry and land cover classification**

190 Nine sets of high-resolution optical images with a geometric resolution of 0.09-0.5 m derived
191 from aerial surveys between 1998 and 2019 (Table 1) were available for land cover analyses.
192 For the years 2003, 2006, and 2009, the planimetric accuracy of single point measurements is
193 better than ± 20 cm (Kaufmann et al., 2015). Comparable planimetric accuracies can be
194 expected for the other stages. The optical data sets were used for visual classification using a
195 hierarchical interpretation key following a scheme developed for Pasterze Glacier by Avian et al.
196 (2018) for laserscanning data and modified later for optical data by Krisch and Kellerer-
197 Pirklbauer (2019, Table 2 therein). Land cover classification was accomplished at a scale of

198 1:300 (for the stages 1998-2015; data based on Krisch and Kellerer-Pirklbauer, 2019) or 1:200
199 (2018-2019; this study). The classification results for a 1.77 km² area at Pasterze Glacier were
200 published earlier by Krisch and Kellerer-Pirklbauer (2019, [Fig. 3 therein](#)) for 1998, 2003, 2006,
201 2009, 2012, and 2015. For a 0.37 km² area, manual land cover classification was accomplished
202 in this study for 2018 and 2019 using the same mapping key.

203

204 **3.3. Terrestrial laserscanning**

205 The glacial-proglacial transition zone of Pasterze Glacier has been monitored by terrestrial
206 laserscanning (TLS) since 2001 from the scanning position Franz-Josefs-Höhe (FJH). The area of
207 interest in the scan sector covers 1.2 km² (Fig. 1a). Using scanning position FJH, one minor
208 limitation of TLS-based data for glacier lake delineation is the oblique scan geometry causing
209 data gaps due to scan-shadowed areas (Avian et al., 2018; 2020). Until 2009 the Riegl LPM-2k
210 system was used followed by the Riegl LMS-Z620 system since then. Technical specifications
211 regarding the two Riegl laserscanning systems as well as the configuration of the geodetic
212 network (scanning position and reference points) can be found in Avian et al. (~~2007~~; 2018).
213 Processing and registration of the TLS data ([point clouds](#)) was performed in Riegl RiScan,
214 subsequently DTMs (with 1 or 0.5 m grid resolution) were calculated in Golden Software Surfer.
215 In this study we used the DTMs to delineate the water bodies in the scan sector manually (for
216 details see Avian et al., 2020) supported by ~~GPS~~-GNSS data (cf. above) for the glacier boundary.
217 [In addition, the point clouds acquired by TLS were used to quantify lake level variations \(see](#)
218 [section 3.4\).](#)-TLS-data from 2010 to 2017⁹ (13.09.2010, 27.09.2011, 07.09.2012, 24.08.2013,

219 09.09.2014, 12.09.2015, 27.08.2016, ~~and~~ 22.09.2017, [13.09.2018](#), and [03.08.2019](#)) were
220 ~~used~~ [analysed](#).

221
222 Furthermore, we quantified ice-surface elevation changes of Pasterze Glacier near the
223 proglacial lake using TLS-data from 13.09.2018 and 03.08.2019. This was done to bring ice
224 volume losses by ablation at the lake-proximal part of the glacier in relation to ice mass losses
225 by buoyant calving for the period of (roughly) August 2018 to August 2019 (see below).
226 Although this data set does not cover an entire glaciological year, at least information about the
227 order of magnitude of the spatially distributed direct ice mass losses by subaerial ablation near
228 the shores of Lake Pasterzensee is gained. The emergence velocity as well as the general glacier
229 motion at the glacier terminus is close to zero (Kellerer-Pirklbauer et al., 2008; Kellerer-
230 Pirklbauer and Kulmer, 2019) apart from ice movement related to crevasses or steeper sloping
231 areas (Seier et al., 2017). Therefore, we can assume that surface elevation changes at the
232 glacier terminus between the two stages equals basically glacier ablation.

233

234 **3.4. Time-lapse photography**

235 At Pasterze Glacier six remote digital cameras (RDC) are installed to monitor mainly
236 glaciological processes with a very high temporal resolution (see Avian et al., 2020; overview
237 regarding the six cameras). One time-lapse camera was operated by the Grossglockner
238 Hochalpenstraße AG (GROHAG) using a Panomax system. The model used is a Roundshot
239 Livecam Generation 2 (Seitz, Switzerland) with a recording rate of mostly 5 minutes during
240 daylight. Time specification is UTC+2. The camera is installed at the Franz-Josefs-Höhe lookout

241 point (Fig. 1a) at an elevation of 2380 m asl and, thus, 310 m above the present lake level of
242 Lake Pasterzensee. Based on this optical data, Kellerer-Pirklbauer et al. (2017) reported a
243 sudden ice-disintegration event at the glacier lake in September 2016 where tilting, lateral
244 shifting, and subsidence of the ground accompanied by complete ice disintegration of a debris-
245 covered ice body occurred. For this study, we visually checked all available Panomax images
246 from 2016 to 2019. Four large-scale and rapidly occurring ice-breakup events (IBE) were
247 detected in the period September 2016 to October 2019 (IBE1: 20.09.2016; IBE2: 09.08.2018,
248 IBE3: 26.09.2018, IBE4: 24.10.2018). The effects on the proglacial landscape during these four
249 IBE was quantitatively analysed as follows.

250

251 For the orthorectification process of the Panomax images (7030x2048 px) it is necessary to find
252 a suitable mathematical model. To get the necessary parameters for this model, control points
253 are needed which are visible in both the Panomax images and pre-existing orthophotos used
254 for the orthorectification process. We applied an interpolation approach using the rubber
255 sheeting model in ERDAS IMAGINE 2018. This model calculates a Triangulated Irregular
256 Network (TIN) for all control points at the reference orthophoto and at the Panomax image and
257 transforms the calculated triangles of the oblique images in such a way that they equal the ones
258 of the reference orthophoto. First degree polynomials were used for the transformation within
259 the triangles. Only control points at the lake level were utilized to achieve a maximum accuracy
260 at lake-level objects. Reasons for minor geometric errors in the analysed orthorectified images
261 were changes in the lake level or an offset of the camera (maximum of 5 pixels). ~~Direct lake~~
262 ~~level measurements at Lake Pasterzensee between 25.06.2019 and 12.09.2019 indicate an~~

263 ~~amplitude of 95 cm (temperature range 0.9–1.8°C) in the 80-day period (pers. comm. Jakob~~
264 ~~Abermann), thus,~~
265
266 To assess the potential effect of lake level changes on geometric errors in the orthorectified
267 images, we quantified lake-level variations by using GNSS and TLS data. We compared lake-level
268 data from nine different GNSS campaigns over a 5-year period (17.09.2015-22.09.2020; all from
269 the period between 11 am to 3 pm). Geometric accuracy is in the range of centimetres based
270 on comparison with stable points. Results yield a mean elevation of 2069.54 m asl ranging from
271 2069.87 asl (17.09.2015) to 2069.19 m asl (22.09.2020), thus a range of 0.68 m with a tendency
272 of lake-level lowering over time (Fig. 4c). In addition, we measured the elevation of small and
273 fresh-looking lake terraces next to the glacier terminus on 14.09.2020 with GNSS yielding an
274 elevation range of 0.59 m. This small elevation range is also in accordance with the lake-level
275 elevations measured by GNSS during two consecutive field campaigns on 14.09.2020 and
276 22.09.2020 with a difference of 0.53 m. TLS-based lake level estimation was accomplished for
277 six dates in the period 2014-2019 (see section 3.3.) by identifying the lowest level of the point
278 cloud at the lake shore (mean elevation of lower most measurement points at the lake shore).
279 Based on TLS data we observed a lake level variation in the order of 0.8 m and a trend in lake
280 level lowering during this period. Therefore, as judged from our long-term as well as short-term
281 GNSS and TLS data, we demonstrate rather stable lake-outflow as well as lake-level conditions
282 at least for the period 2015-2020 with a lake-level lowering trend. The assumption of long-term
283 lake level variations <1 m during the summer months (seasonal amplitude) is further supported
284 by field observations during the last years with the shape (stepped geometry) and size (< 1m

285 vertical extent) of thermo-erosional notches at the waterline. Therefore, the potential effect of
286 lake level changes on geometric errors in the orthorectified images should be small.

287
288 Three groups of control points were generated using the three pre-existing orthophotos of
289 11.07.2015, 11.09.2018, and 15.11.2018 (Table 1) and suitable Panomax images from the same
290 days. For the IBE1 we used the model of 11.07.2015, for IBE2 and IBE3 the model of
291 11.09.2018, and for IBE 4 the one of 15.11.2018. The calculated orthorectified images have a
292 geometric resolution of 0.2 m. ArcGIS 10.5 was subsequently used to analyse landform changes.

293 ~~For more details see Bernsteiner (2019).~~

294

295 **3.5. Quantification of Quantification of ice mass losses by buoyant calving**

296 A quantification of ice losses by buoyant calving was attempted by using the Panomax images.
297 Three of the large-scale ice-breakup events occurred between August and September 2018
298 (IBE2 to IBE4). For these events we estimated the volume of the newly emerging icebergs and
299 the volume of uplifted ice masses detaching from the subaquatic glacier ice. The latter was
300 accomplished by comparing the calculated volume of a given ice-mass (e.g. a debris-covered ice
301 slab) before and after the ice-breakup event. For volumetric calculations we applied the
302 following approach. The horizontal extent of affected (newly emerged or uplifted) ice masses
303 was transferred back to and drawn into the original webcam images. A maximum iceberg
304 height was also drawn as a line in the original webcam image. The length of this line was then
305 quantified by using the ratio between the quantified horizontal extent and the marked line. The
306 iceberg height then was obtained by applying a correction calculation for the camera distortion

307 produced by an incidence angle of 25° (calculated by a height difference of 310m and a
308 horizontal distance of approx. 650m).

309
310 The volume of individual icebergs was approximated by assuming that all ice bodies above the
311 waterline have the form of a truncated pyramid, where A₂ is 20% (for dome-shaped iceberg),
312 50% (for mixed iceberg type) or 80% (for tabular iceberg) of A₁. The volume of truncated
313 pyramid (iceberg above the waterline) with irregular base is given by

314
315
$$V = \frac{h}{3} (A_1 + \sqrt{A_1 * A_2} + A_2) \quad (1)$$

316
317 with A₁ = area at the waterline (larger base), A₂ = area of the top face (smaller base; in our cases
318 20, 50 or 80% of A₁ depending on iceberg type), and h = maximum height of iceberg or
319 truncated pyramid (Harris and Stöcker, 1998). With this approach we quantified the volume of
320 nine icebergs for IBE2 (09.08.2018), eight for IBE3 (26.09.2018), and two for IBE4 (24.10.2018),
321 respectively. The volume above the waterline was then multiplied by 10 to calculate the total
322 iceberg volume. Significant uncertainties in this quantification attempt are the visual and thus
323 subjective estimation of the iceberg height and the fact that only large icebergs are considered.
324 Therefore, results of this approach must be seen only as order of magnitudes of ice mass losses
325 by buoyant calving in the period 09.08.2018 to 24.10.2018.

326

327 **3.56. GeophysicsElectrical resistivity tomography**

328 Electrical resistivity tomography (ERT) and seismic refraction (SR) has been applied in the study
329 area between 2015 and 2019. For space reasons, we focus only on selected aspects of the ERT
330 results in this paper. Electrical resistivity is a physical parameter related to the chemical
331 composition of a material and its porosity, temperature, water and ice content (Kneisel and
332 Hauck 2008). For ERT a multi-electrode and multichannel system (GeoTom 2D system, Geolog,
333 Germany) and two-dimensional data inversion (Res2Dinv) using finite difference forward
334 modelling and quasi-Newton inversion techniques (Loke and Parker, 1996) was applied. ERT
335 was carried out at a total of 43 profiles (3 in 2015, 4 in 2016, 4 in 2017 [Fig. 3a,b], 5 in 2018, and
336 27 in 2019 [Fig. 3c]) with 2 or 4 m electrode spacing and profile lengths of 80-196 m. Salt water
337 was sometimes used at the electrodes to improve electrical contact. RTK-GNSS was applied to
338 measure the position of each electrode and thus the course of the profile (Fig. 3b). We applied
339 in most cases both the Wenner and Schlumberger arrays (Kneisel and Hauck, 2008). Focus is
340 given here on the Wenner results, which are more suitable for layered structures (Kneisel and
341 Hauck 2008). ERT data from 2015 and 2016 were taken from Hirschmann (2017) and Seier et al.
342 (2017). The apparent resistivity data were inverted in Res2Dinv using the robust inversion
343 modelling. ERT data were checked before processing for abnormally high or low resistivity
344 values. Abnormal values are commonly related to measurement errors and/or bad electrode
345 contact usually visible at all depths. Such ‘bad datum points’ were excluded manually (Kneisel
346 and Hauck, 2008).~~Bad datum points were removed before the inversion.~~ The number of
347 iterations was stopped when the change in the RMS error between two iterations was small.
348 ~~(Locke, 2000).~~
349

350 **3.67. Bathymetry**

351 Sonar measurements were carried out at Lake Pasterzensee at the 13.09.2019. Water depth in
352 the lake was measured with a Deeper Smart Sonar CHIRP+ system (depth range 0.15-100 m)
353 consisting of an echo sounding device (single-beam echo sounder) and a GNSS positioning
354 sensor. CHIRP stands for Compressed High Intensity Radar Pulse. We measured with 290 kHz
355 (cone angle 16°) and a sonar scan rate of up to 15/second. According to the producer, the 16°
356 beam angle of the 290 kHz frequency results in a ground footprint of 0.28 m at 1m water depth,
357 of 2.81 m at 10 m water depth and of 11.24 m at 40 m water depth. These footprint values are
358 not optimal for resolving small-scale features at large water depths. However, as it was
359 intended in this study, the footprint values are acceptable for getting an overview of the lake
360 geometry.

361

362 The accuracy of raw water-depth measurements depends on the used device, beam angle,
363 sonar stability, bottom composition, and structure. Bandini et al. (2018) compared the Deeper
364 Smart Sensor PROx system (precursor of CHIRP+) against the ground truth. Their results
365 indicate a mean absolute error of 0.52 m for water depths of up to 30 m with almost perfect fit
366 (ground truth vs. sonar) at shallow sites. The tested PROx system underestimated the water
367 depth attributed to the beam diameter as it tends to take the shallowest point in the beam as
368 the depth reading when going over holes or slopes. No such comparative studies are published
369 for the CHIRP+ system. However, according to the producer the absolute error should be lower
370 for the CHIRP+ (pers. comm. by the technical support of Deeper, 16.12.2020). In conclusion, the

371 estimated accuracy of raw water-depth measurements should be less than 0.1 m at shallow (<5
372 m) and flat sites but might be as high as 0.5 m for deeper and sloping locations.

373
374 ~~Sonar measurements were carried out at Lake Pasterzensee at the 13.09.2019. Water depth in~~
375 ~~the lake was measured with a Deeper Smart Sonar CHIRP+ system (depth range 0.15–100 m)~~
376 ~~consisting of an echo sounding device and a GPS positioning sensor. The estimated accuracy of~~
377 ~~raw water depth measurements should be less than 10 cm according to the manufacturer.~~The

378 CHIRP+ system ~~system~~ was mounted on a Styrofoam platform for stability reasons and dragged
379 behind a small (and rather unstable) inflatable canoe operated by two people. Altogether 4276
380 water depth measurements along a 4.3 km long route were accomplished (Fig. 1d) ~~measuring~~
381 ~~with 290 kHz (cone angle 16°)~~. Because icebergs and wind cause boat instability, the canoe was
382 not navigated along a regular shore-to-shore route but rather in a zigzag mode starting in the
383 northwest of the lake and ending in the southeast. GPS-GNSS and water depth data were
384 imported into ArcGIS for further analysis. To compute the lake geometry, the measured lake
385 depth values and a lake mask of September 2019 were combined using the Topo to Raster
386 interpolation tool to calculate a digital terrain model (DTM) with a 5m grid resolution. Lake
387 volume was calculated using the functional surface toolset.

388

389 **4. RESULTS**

390 **4.1. Glacier recession and areal expansion of the lake**

391 Figure 4a depicts the terminus positions between 1998 and 2019 as well as the proglacial water
392 surfaces including Lake Pasterzensee and the proglacial basin as defined for September 2019

393 (area of 0.365 km²). The glacier steadily receded into the current proglacial basin over a
394 longitudinal distance of about 1.4 km. In detail, however, this recession was not evenly
395 distributed along the glacier margin due to differential ablation below the uneven supraglacial
396 debris. The east part of the glacier tongue receded up-valley beyond the proglacial basin. The
397 west part of the glacier tongue is still in contact with the proglacial lake and changed
398 morphologically rather little during the last two decades. Figure 4a also depicts 100 m wide
399 strips where mean values for longitudinal and lateral backwasting were calculated. Results are
400 shown in Fig. 4b. The longitudinal backwasting rate was between 29.0 and 217.2 m yr⁻¹, 2 to 19
401 times larger than the lateral backwasting rate of 7.3 to 13.2 m yr⁻¹. High annual longitudinal
402 backwasting rates were measured in most years when the glacier was in the basin. Since 2017,
403 this rate drastically dropped, presumably due to the detachment of the glacier from the lake.

404

405 Figure 5 illustrates glacier recession and the evolution of proglacial water bodies for the period
406 1998-2019 in relation to the 0.365 km² proglacial basin as defined for September 2019. An
407 animation showing the general evolution of the proglacial lake between 2010 and 2020 is
408 published in the supplement. In 1998 only 0.5% of the basin was covered by water (Fig. 5a). Up
409 to 2006, water surfaces still covered less than 5% of the basin (Fig. 5c). By 2009, this value
410 increased to 11.2% (Fig. 5d) and was rather constant until two years later (Fig. 5f). By 2016,
411 more than 50% of the basin was covered by water (Fig. 5k) and in 2019 water surfaces in the
412 basin covered 83.2% (Fig. 5n). The increase in water surface areas in the basin since 1998
413 follows an exponential curve (Fig. 6a). However, in single years this areal increase follows a
414 distinct pattern with enlargement of water surfaces during summer and a decrease in autumn

415 due to lake level lowering as revealed by field observations. The exceptionally low value of
416 November 2018 (62.4%) in relation to September 2018 (73.2%) is related to the widespread
417 existence of ice floes. Figure 6a also depicts the extent of icebergs in the proglacial basin with
418 values below 1% in most cases. High percentage values were only mapped for 15.11.2018
419 (7.3%) ~~suggesting~~ followed by rapid iceberg loss during the ablation season 2019.

420

421 **4.2. Land cover change in the lake-proximal surrounding since 1998**

422 Different glacial and proglacial surface types and landforms were mapped for a 0.76 km² area in
423 the glacial-proglacial transition zone for nine different stages between 1998 and 2019 (Fig. 7).
424 The visual landform classification gives a more detailed picture on landform changes in the area
425 of interest. Figure 6b quantitatively summarises the relative changes of different surface types
426 in this transition zone. Debris-poor, rather clean-ice covered 58% of the area in 1998, decreased
427 to 9.3% until 2015, and vanished afterwards from the area. In contrast, debris-rich glacier parts
428 covered in all nine stages between 20.5% (2019) and 33.4% (2015) of the transition zone. For
429 this class, areal losses due to glacier recession were partly compensated by areal gains due to
430 an increase in supraglacial debris-covered areas. Water surfaces increased from 2.1% in 1998 to
431 45.5% in 2019. The low value for 15.11.2018 is related to ice floes (3.4%), data gaps (4.1%), as
432 well as high values for both debris-rich (2.1%) and debris-poor (1.5%) icebergs. Areas covered
433 by bedrock and vegetation were always around 4%. Areas covered by fine-grained sediments
434 reached a maximum in 2012 decreasing substantially afterwards (mainly due to lake extension).
435 Areas covered by coarse-grained sediments increased from 3.3% in 1998 to about 26-27% in
436 2018 and 2019 and are located at the northern and eastern margin of the basin. Finally, dead

437 ice holes were mapped for all stages, but their spatial extent was always very small (maximum
438 in 2012 with a total area of 618 m²) and covered less than 0.1% of the basin.

439

440 **4.3. Buoyant calving at the ice-contact lake**

441 Four large-scale ice-breakup events (IBE) related to buoyancy were detected for the period
442 September 2016 to October 2019 (IBE1: 20.09.2016; IBE2: 09.08.2018, IBE3: 26.09.2018, and
443 IBE4: 24.10.2018). Twelve smaller to mid-sized iceberg-tilting or capsize events were
444 additionally documented by the Panomax images (27.05.2017, 28.05.2017, 09.06.2017,
445 11.06.2017, 20.06.2017, 05.07.2017, 19.07.2017, 25.09.2017, 22.06.2018, 23.09.2018,
446 26.09.2018, and 30.10.2018).

447

448 IBE1 occurred on 20.09.2016. Figure 8a presents two ortho-images from this event at its
449 beginning (9:00 am) and its end (11:15 am). The latter also indicates the position of the
450 geoelectric profile ERT17-1 for orientation. Figure 2 visualizes the same event. [An animation](#)
451 [depicting this ice-breakup event is published in the supplement.](#) Different processes occurred
452 as indicated by the capital letters in Fig. 7a: Limnic transgression (A and F) of water due to
453 tilting of ice slabs, uplift of a debris-covered ice slab (B and G), formation of a massive crevasse
454 (C), complete ice disintegration (D), ice disintegration and lateral displacement of several ice
455 slabs (E), and drying out of a meltwater channel (H). All processes apart from the limnic
456 transgressions ended by 11:15 am, the latter terminated at 3:30 pm. The formation of the large
457 crevasse started initially at 9:30 am, followed by a rapid widening until 9:45 am (crack width 3.5
458 m), steady conditions until 10:45 am, followed by a second widening phase (crack width 5.5 m)

459 until 10:50 am (see inset graph in Fig. 8a). The morphologically most distinct event happened
460 between 9:50 am (Fig. 2d) and 9:55 am (Fig. 2e) when the total collapse of a 1700 m² large ice
461 slab occurred accompanied by lateral shift and tilting of neighbouring ice slabs by lateral push
462 (E) and lowering of the surface of previously tilted slabs (B).

463
464 IBE2 happened on 09.08.2018. Figure 8b depicts the changes that occurred between 4:35 pm
465 and 4:58 pm. At this event three different processes were identified: (A) detachment of a
466 debris-covered ice peninsula (945 m²) from Pasterze Glacier at the western lakeshore and
467 separation into four icebergs (total area 1054 m²), (B) emergence of a 1035 m² large iceberg
468 (4:35-4:40 pm) followed by capsizing and partially disintegration of this iceberg into ice debris
469 (4:40-4:58 pm) pushing away other icebergs which cause (C) lateral iceberg displacement of up
470 to 65.6 m as well as a clockwise iceberg rotation of 95°.

471
472 IBE3 occurred on 26.09.2018. This event involved four main processes as visualised in Fig. 8c:
473 (A) uplift of debris-covered ice bodies increasing the surface area from 6820 to 13245 m² in
474 only 10 minutes (at 2:35-2:45 pm), (B) emergence of a new iceberg between 2:35 and 2:40 pm
475 which capsized a few minutes afterwards, (C) limnic transgression, and (D) lateral iceberg
476 displacement (both at 2:35-3:00 pm). At the southern part of the affected area, icebergs moved
477 away from the uplifting area (push effect). In contrast, at the eastern part of the affected area
478 icebergs moved towards the uplifting area possibly due to compensatory currents causing a
479 suction effect. A large iceberg (IB1 in Fig. 7c) was hardly moving at all suggesting grounding
480 conditions.

481

482 The last major IBE took place on 24.10.2018 (IBE4) spanning only 5 minutes (Fig. 8d). Like IBE2,
483 a debris-covered ice peninsula (1,933 m²) detached from Pasterze Glacier at the western
484 lakeshore and separated into several icebergs (A). Furthermore, (B) ice disintegration and (C)
485 lateral iceberg displacement was observed during the event. The large iceberg IB1 experienced
486 a lateral offset of 22 m accompanied by a clockwise rotation by 43°. Spatial extent, volume and
487 freeboard of this iceberg were calculated based on a high-resolution DTM derived from the
488 aerial survey dating to 15.11.2018 (cf. Table 1). The subaerial volume of iceberg IB1 was 3271
489 m³ on 15.11.2018, which should be around 10% of the entire iceberg. Hence, some 29,500 m³
490 (90%) were during that time below the lake level. Maximum freeboard of IB1 was 3.7 m with a
491 mean freeboard value of 1.4 m. If we assume the same surface area of the iceberg below lake
492 level (2287 m²), we could further assume a mean ice thickness of the iceberg of 14.3 m (12.9 m
493 draft, 1.4 m freeboard). Therefore, in order to have a freely moveable iceberg, a water depth
494 exceeding 13 m is needed.

495

496 No large buoyant calving events were detectable in the time-lapse images after 24.10.2018.

497 However, at least the occurrence of small-sized buoyant calving events which are hardly

498 detectable by the time-lapse camera can be assumed. During field work in June 2019, we

499 observed buoyant calving of a small, c.3 m long iceberg ("shooter") according to Benn and

500 Evans, 2010) c.200 m from the subaerial glacier front (Fig. 3d). The whole event took only few

501 minutes and was hardly visible in the time-lapse images of that particular day.

502

4.4. Ice mass loss by buoyant calving and subaerial ablation

The quantification of the ice loss by buoyant calving for the three events IB2 to IB4 approximated by ice detachment, uplift and emergence processes revealed the following results. The sum of movement-affected ice masses (without lateral displacement) during the three ice-breakup events were 55,717 m³ for IBE2, 445,257 m³ for IBE3, and 537,604 m³ for IBE, respectively, summing up to 1,038,578 m³ (Table 2). As no other substantial ice break-up events occurred afterwards, we can therefore assume that ice loss by buoyant calving in the period August 2018 to August 2019 at Pasterze Glacier was at least in the order of 1×10^6 m³.

The comparison of the two sets of TLS-data from 13.09.2018 and 03.08.2019 revealed surface elevation changes and thus more or less glacier ice ablation of up to 5 m between the two stages. It was not the scope of this paper to analyze ablation rates at the terminus of Pasterze Glacier in detail. However, for a rough estimate we can calculate for the lowest part of the glacier tongue next to the proglacial lake (see Fig. 1, c.0.35 km²) the total ice loss for the period September 2018 to August 2019. Mean ablation rates of 2.5 m or 3.0 m for this area would yield total ice losses by ablation for this area of 870,000 m³ and 1,050,000 m³, respectively.

4.4.5. Ground ice conditions at the lake basin and its proximity

Altogether 43 ERT profiles were measured in the proglacial area between 2015 and 2019 with profile lengths of between 80 and 196 m. In this study we focus on the quantification of sediment-buried dead ice bodies detected by ERT. A detailed discussion on the ERT results will

525 be presented elsewhere. Resistivity values $>20,000$ Ohm m indicate buried glacier ice and
526 water-saturated glacial sediments show values $<3,000$ Ohm m (Pant and Reynolds, 2000). Clay
527 and sand have resistivity values in the ranges of 1-100 and 100-5,000 Ohm m, respectively.
528 Temperate glacier ice may exceed 1×10^6 Ohm m (Kneisel and Hauck, 2008). We used the
529 20,000 Ohm m-boundary in the interpretation to estimate the maximum ice thickness for each
530 profile as depicted in Fig. 9 which shows three profiles from 2017. In many cases, ice thickness
531 exceeded the depth of ERT penetration. Therefore, we only were able to calculate "minimum
532 ice thickness estimates" based on the ERT data.

533
534 Figure 10 summarises the results of the surveys for 2015, 2016, 2017, 2018 and September
535 2019. Two of the three ERT profiles measured in 2015 (ERT15-1, ERT15-2) revealed only very
536 thin ice lenses. Both are located outside the proglacial basin as defined in September 2019 (Fig.
537 10a). The profile in the basin had an estimated ice thickness of 14 m (ERT15-3). The profiles
538 measured in 2016 revealed minimum ice thickness values of 8-10 m (Fig. 10b). The four profiles
539 measured in 2017 in the central part of the proglacial area revealed minimum ice thicknesses of
540 between 13 (ERT17-4) and 28 m (ERT17-2) (Fig. 10c) confirming the existence of massive dead
541 ice beneath a thin veneer of debris (Fig. 9).

542
543 The interpretation of four profiles measured in 2018 are shown in Fig. 10d. Profiles ERT18-2 and
544 ERT18-3 are free of ice located outside the basin or at its margin. ERT18-4 and ERT18-5 were
545 both located in the basin and revealed minimum ice thicknesses of 13 (ERT18-5) and 14 m
546 (ERT18-4). The September-2019 measurements supported earlier measurements (Fig. 10e). The

547 profiles at the eastern margin of the basin showed again a thin layer (ERT19-18; 8m ice) or only
548 very small occurrences of glacier ice (ERT19-19; 1 m ice). The three profiles near the north-
549 western shore of the lake revealed minimum ice thickness estimates of up to 26 m (ERT19-26).
550 In summary, ERT profiles outside the proglacial basin typically showed little buried dead ice
551 remnants, whereas profiles in the basin (particularly at its north-western part) typically yielded
552 resistivity values consistent with widespread massive dead ice.

553

554 **4.56. Bathymetry of the lake basin**

555 Lake bottom geometry and water volume of Lake Pasterzensee was calculated based on 4276
556 sonar measurements (Fig. 1d). Measured water depths ranged from 0.35 m to 48.2 m yielding
557 an arithmetic mean of 13.4 m and a median of 10.7 m. During the time of bathymetric
558 measurements, the lake level was 2069.1 m asl implying that the lowest point at the lake
559 bottom was 2020.9 m asl (Fig. 11a). Several sub-basins (marked as A-D in Fig. 11a) were
560 identified along the 1.2 km long and up to 300 m wide lake basin. One small sub-basin (A) was
561 detected close to the southern end of the lake with maximum measured water depths
562 exceeding 20 m (maximum 24.1 m, 2045 m asl), an E-W extent of 160 m, and a N-S dimension
563 of 140 m. A second sub-basin (B) is slightly less deep (max. 20.5 m) but seems to be broader
564 compared to basin (A). The third sub-basin (C) is by far the deepest, the largest, and the most
565 complex one with a maximum water depth of 48.2 m and a secondary basin in the south
566 reaching a measured maximum depth of 31.0 m. In this sub-basin, water depths exceeding 30
567 m were calculated for a 34,000 m² large in the central part of the entire lake basin. The lake
568 basin gets generally shallower towards the northwest. Finally, a fourth sub-basin (D) was

569 identified at the north-western end of Lake Pasterzensee where a broad basin is located with a
570 maximum measured depth of 17.7 m. Based on our gridded DTM for the lake bottom, the
571 estimated water volume of the 299,496 m² large Lake Pasterzensee in September 2019 was 4 x
572 10⁶ m³. The gradient from the deep basin (C) to the shore seems to be rather gradual at the
573 eastern margin of the lake. In contrast, at the western margin of the lake basin where Lake
574 Pasterzensee is in ice-contact, the gradient is steep in most areas (e.g. at sub-basin C: horizontal
575 distance between sonar measurement location and glacier margin 19 m vs. water depth 26.1m)
576 suggesting a steep glacier margin with a pronounced ice foot.

577

578 **5. DISCUSSION**

579 **5.1. Glacial-to-proglacial landscape modification**

580 Pasterze Glacier receded by some 1.4 km between 1998 and 2019 thereby causing the
581 formation of a bedrock-dammed lake in an over-deepened glacial basin. During these two
582 decades, the glacier decelerated, fractured (Kellerer-Pirklbauer and Kulmer, 2019) and lost the
583 connection to the lake at its eastern part. In contrast, at the western shore, the lake was still in
584 ice contact with the glacier in 2019. This ice-contact difference is related to an unequal
585 recession pattern of the eastern and western part of the glacier tongue caused by an uneven
586 distribution of the supraglacial debris cover (Kellerer-Pirklbauer, 2008). The debris cover
587 distribution pattern promotes differential ablation (Kellerer-Pirklbauer et al., 2008). Rapid
588 deglaciation as well as glacier thinning is much more intensive at the debris-poor part of the
589 glacier affecting the stress and strain field and modifying the flow directions of the ice mass

590 (Kaufmann et al., 2015). Therefore, the proglacial lake predominantly developed in areas where
591 debris-poor ice was located before.

592
593 At the waterline, thermo-erosional undercutting causes the formation of notches (cf. Röhl,
594 2006). Such notches are frequent features at Pasterze Glacier, and were first reported in 2004
595 (Kellerer-Pirklbauer, 2008). DPGS measurements at the glacier margin on 13.09.2019 showed
596 that waterline notches occurred during that time at 53% of the 935 m long ice-contact line
597 between Pasterze Glacier and Lake Pasterzensee (Fig. 5n). Notches observed at Pasterze Glacier
598 during several September-field-campaigns during the last years had a stepped geometry due to
599 lake-level drop. The amplitude of water-level fluctuations at Pasterzensee in the period 2015 to
600 2020 is/was in the order of one less than a meter based on GNSS and TLS data indicating rather
601 stable lake-outflow conditions. However, GNSS and TLS data both show a lake-level lowering
602 trend since 2015. -meter during the summer months as shown by lake level measurements
603 (pers. comm. Jakob Abermann; cf. methods section).

604
605 Stepped geometries were observed also at other alpine lakes (e.g. Röhl 2006). Rates of notch
606 formation and, thus, thermo-erosional undercutting at Pasterze Glacier are unknown. However,
607 if we consider the annual lateral backwasting rates derived from ~~DPGS~~ GNSS data (Fig. 4) as
608 indicative for thermo-erosional undercutting, a mean melt rate of about 10 m yr⁻¹ for the period
609 2010-2019 can be assumed. This is about one third of the values quantified for Tasman Glacier
610 (Röhl, 2006). The difference is possibly related to cooler (higher elevation) and more shaded
611 (NE-facing) conditions at Pasterze Glacier. Outward toppling of undercut ice masses due to

612 thermal erosion, a process potentially relevant for calving at ice-contact lakes (Benn and Evans
613 2010), was not observed at Pasterze Glacier. Lateral backwasting at Pasterze Glacier is mainly
614 controlled by ice melting either beneath supraglacial debris or at bare ice cliffs above notches
615 where the slope is too steep to sustain a debris cover and thus the rock material slides into the
616 lake (see Fig. 10 in Kellerer-Pirklbauer, 2008).

617

618 The analysis of the relationship between glacier recession and the evolution of proglacial water
619 surfaces showed drastic changes in 1998-2019. The spatial extent of water surfaces in the 0.37
620 km² proglacial basin followed an exponential curve with 0.5% water surfaces in 1998, 21% by
621 2013, 51% by 2016, and 83% by 2019. On an annual timescale water surface changes follow a
622 distinct pattern with enlargement during summer due to glacier and dead-ice ablation in lake-
623 contact locations causing lake transgression and a shrinkage in size in autumn due to lake level
624 lowering. This annual pattern at Lake Pasterzensee has been also detected and quantified by
625 Sentinel-1 and Sentinel-2 data (Avian et al., 2020).

626

627 Carrivick and Tweed (2013) discuss the enhanced ablation at ice-contact lakes via mechanical
628 and thermal stresses at the glacier-water interfaces. They report increasing lake sizes in the
629 proglacial area of Tasersuaq Glacier, west Greenland, for four different stages between 1992
630 and 2010. An exponential increase in lake size, as observed at Pasterze Glacier, was however
631 not observed at Tasersuaq Glacier as judged from their provided map in the paper. More
632 general, detailed studies of increasing lake size on an annual basis are rare impeding the

633 comparison of our results with other studies accomplished in similar topoclimatical settings.
634 Some comparative observations are, however, as follows.
635
636 Schomacker and Kjær (2008) report from a glacier in Svalbard that an ice-contact lake increased
637 near-exponentially in size during a period of 40 years due to dead-ice melting. Schomacker
638 (2010) report from the enlargement of proglacial lakes at Vatnajökull in Iceland where the lake
639 Jökulsárlón enlarged by 40% in only 9 years (2000-2009). For the same lake, Canas et al. (2015)
640 revealed an enlargement by 74% for the period 1999-2014. Stokes et al. (2007) report an 57%
641 increase in the surface area of supra- and proglacial lakes in the Caucasus Mountains in the
642 period 1985-2000. Loriaux and Casassa (2012) described the evolution of glacial lakes from the
643 Northern Patagonia Icefield reporting a total lake area increase of 64.9% in a 66-year period
644 (1945-2011). Gardelle et al. (2011) detected for the Eastern Himalaya an enlargement of glacial
645 lakes by 20% to 65% between 1990 and 2009. To conclude, the numbers summarised here
646 clearly show that the increase in lake size at Pasterze Glacier is particularly high although this
647 relative increase in area at Lake Pasterzensee is likely biased by the very small initial size of the
648 lake in 1998.
649
650 Landscape changes were quantified for a 0.76 km² large transition zone between Pasterze
651 Glacier and its foreland for the period 1998-2019. Apart from rapid deglaciation and lake size
652 increase, areas covered by coarse-grained glacio-fluvial sediments increased in their extent.
653 Furthermore, icebergs in the lake were mapped for the first time in 2015 (0.7% of the 0.76 km²
654 large area) and reached their maximum extent in 2018 (3.5%). By the end of the ablation

655 season in 2019, the areal extent of icebergs decreased dramatically to only 0.3% attributed to
656 high melt rates in a warm summer 2019 (Fig. 1c: the MAAT in 2019 was the second highest in
657 the period 1998-2019). After 2015, an alluvial fan with a lake delta developed at the northern
658 end of the lake because the glacier receded at this location from the lake basin connecting the
659 main glacial stream directly with the lake (Fig. 6f and g). This recession was, however, only
660 superficial, and huge amounts of dead ice remained in the basin – as detected by ERT
661 measurements – and were covered by fluvio-glacial sediments.

662

663 **5.2. Dead-ice conditions and changes**

664 Subsurface conditions at the proglacial area of Pasterze Glacier were studied by measuring
665 electrical resistivity along 43 profiles distributed over the entire proglacial area between 2015
666 and 2019. Our measurements showed that dead ice bodies covered by sediments were absent
667 outside the proglacial basin as defined for September 2019. In contrast, all ERT measurements
668 carried out in the basin revealed very high maximum and median resistivity values (e.g. Fig. 9)
669 indicative of buried ice. Long-term air temperature data from a nearby automatic weather
670 station as well as two ground temperature data series directly from the proglacial area clearly
671 suggest that permafrost is absent at the shores of Lake Pasterzensee due to permafrost-
672 unfavourable thermal conditions (MAAT always $>2.5^{\circ}\text{C}$ since 2011). Furthermore, a distinct
673 warming trend occurred in the period 1998-2019 at Pasterze Glacier enhancing ice ablation and
674 deglaciation processes at the surface and the surface in more recent years.

675

676 In addition to the geomorphic observations made at the surface such as dead-ice holes (Figs 6b
677 and 7) or cracks (Fig. 2) in hummocky fluvio-glacial sediments (Fig. 3c), our subsurface data
678 clearly suggest substantial and rapid dead-ice degradation at present. Gärtner-Roer and Bast
679 (2019) conclude that only a few attempts have been made to describe and analyse the
680 occurrence, distribution, and dynamics of ground ice in recently deglaciated areas. However,
681 due to the rapid increase in proglacial areas at present, these authors point out that there is
682 increasing interest on research both for geomorphologist and hydrologists. With the presented
683 geophysical data from Pasterze Glacier, we proved the widespread existence of debris-covered
684 dead-ice bodies in a proglacial basin of an alpine valley glacier and, thus, contribute to this
685 emerging topic.

686

687 **5.3. Ice-breakup and buoyant calving**

688 Four remarkable ice-breakup events (IBE) with horizontal extents in the order of hundreds of
689 meters occurred in the period September 2016 to October 2018. No comparable events were
690 observed before the 20.09.2016 (Kellerer-Pirklbauer et al., 2017) and no comparable event
691 happened between 25.10.2018 and 29.07.2020. Only smaller buoyant calving events can be
692 assumed for the latter period as suggested by a fortuitously observed event (Fig. 3d).

693 Approximations of the ice volume lost by buoyant calving as well as by ablation through
694 subaerial melting at the lowest part of Pasterze Glacier have been in the same order of
695 magnitude ($c.1 \times 10^6 \text{ m}^3$) in almost identical periods (for buoyant calving: August 2018 to August
696 2019; for subaerial melting: September 2018 to August 2019). However, as the period August to
697 October 2018 was very unusual in terms of larger ice-breakup events (three of the four large

698 events occurred in this period), we can clearly conclude that multiannual glacier ice losses by
699 buoyant calving are substantial smaller compared to subaerial ablation rates.

700
701 Our field observations show that sediment is present on top of dead ice, particularly at the
702 north-western end of the lake where the main glacial stream enters the lake. Sediment cover
703 will affect the buoyant weight of the ice column, potentially offsetting buoyant forces and
704 inhibiting calving. It is not possible to quantify this effect, due to limited data on sediment and
705 ice thicknesses. It is clear, however, that although sediment cover will have delayed the onset
706 of buoyant calving, it was insufficient to prevent it in this case.

707
708 Thanks to high-resolution (both spatial and temporal) time-lapse photography overlooking the
709 glacial-proglacial transition zone, different ice-related processes can be clearly distinguished.
710 Common features of the IBEs are (a) limnic transgression due to ice slab lowering or tilting, (b)
711 drying out of meltwater channels due to slab uplift or tilting of ice slabs, (c) uplift – and
712 therefore enlargement – of previously existing ice-cored terraces or icebergs, (d) crack and
713 crevasse formation at previously stable-looking terraces, (e) sudden disintegration of ice
714 masses (i.e. collapsing ice masses) within minutes into ice debris, (f) lateral displacement of
715 icebergs (either pushed away or dragged towards uplifting icebergs), (g) emerging new icebergs
716 previously not mapped due to buoyant calving, (h) capsizing of new icebergs, and (i)
717 detachment of “ice peninsulas” attached to Pasterze Glacier at the western lakeshore and
718 subsequent fragmentation into several icebergs and disintegration into small, mainly floating
719 icebergs. Regarding emergence of new icebergs, our observations suggest both buoyant calving

720 of small ice masses (suggested by emerging small icebergs, e.g. Fig. 3d) but also full-thickness
721 ice calving (suggested by the large ice-breakup events; Fig. 8).

722

723 All these processes are related to hydrostatic disequilibrium of the glacier margin or subaquatic
724 dead ice which becomes super-buoyant and subject to net upward buoyant forces (Benn et al.,
725 2007). Buoyant glacier margins can slowly move back into equilibrium by ice creep or can
726 fracture catastrophically as described for instance for Glacier Nef in Chile by Warren et al.
727 (2001). At Pasterze, creep rates are very low at the glacier margin with only few meters per
728 year near the terminus (Kellerer-Pirklbauer and Kulmer, 2019) therefore only the latter option
729 for a renewed hydrostatic equilibrium is feasible. A floating process of the glacier terminus was,
730 however, not observed at Pasterze Glacier (Boyce et al., 2007). Our buoyant calving
731 observations as well as the bathymetric data suggest the existence of an ice foot at the west
732 shore of the ice-contact lake. Such a presence of an ice foot below the water level of tidewater
733 ice cliffs of temperate glaciers has been debated for more than 120 years (Hunter and Powell,
734 1998). At Pasterze Glacier only small ice cliffs above thermo-erosional notches exist. However,
735 the existence of an ice foot at the western shore is very likely. This assumption is supported by
736 the occurrence of the ice breaking events with buoyant calving-related processes.

737

738 In summary, we identified the following sequence of processes at Pasterze Glacier: (a) glacier
739 recession into an overdeepened basin and glacier thinning below spillway-level; (b) glacio-
740 fluvial sedimentation in the glacial-proglacial transition zone covering dead ice; (c) initial
741 formation and accelerating enlargement of a glacier-lateral to supraglacial lake by ablation of

742 glacier ice and debris-covered dead ice forming thermokarst features; (d) increase in
743 hydrostatic disequilibrium leading to general glacier-ice instability; (e) destabilization of debris-
744 buried ice at the lake shore expressed by fracturing, tilting, and disintegration due to buoyancy;
745 (f) emergence of new icebergs due to buoyant calving; (g) gradual melting of icebergs along
746 with iceberg capsizing events. This sequence of processes is visualized in a conceptual model
747 depicted in Fig. 12. Our observations suggest that buoyant calving, previously not reported
748 from the European Alps, might play an important role at alpine glaciers in the future as many
749 glaciers are expected to recede into valley overdeepenings or cirques.

750

751 **6. CONCLUSIONS**

752 We studied the glacial-to-proglacial landscape transformation at the largest glacier in Austria
753 during the period 1998 to 2019 focusing on ice-contact lake evolution and buoyant calving
754 processes in an overdeepened basin. The main conclusions which can be drawn from this study
755 are the following:

- 756 • High annual backwasting rates were measured in most years when the glacier
757 terminated in the basin. The detachment of the glacier from the lake at the east side
758 drastically reduced backwasting rates.
- 759 • Detailed studies of increasing lake size on an annual basis are rare. We showed that the
760 increase in water surfaces in the basin since 1998 follows an exponential curve (1998:
761 1900 m²; 2019: 0.3 km²). The increase in lake size is particularly high although this
762 pattern is likely biased by the very small initial size of the lake in 1998. In single years
763 this areal increase follows a distinct pattern with enlargement of water surfaces during

764 summer and a decrease in autumn due to lake-level lowering supporting earlier
765 satellite-based studies (Avian et al. 2020).

- 766 • Icebergs in the up to 48.2 m deep lake were observed for the first time in 2015 and
767 reached their maximum extent in 2018. By the end of the ablation season in 2019, the
768 areal extent of icebergs decreased dramatically, attributed to high melt rates in a warm
769 summer 2019.
- 770 • Both, geomorphic observations made at the surface and geophysical data from the
771 subsurface clearly suggest widespread existence of debris-covered dead-ice bodies in
772 the proglacial basin which is substantially and rapidly affected by dead-ice degradation
773 at present due to permafrost-unfavourable ground temperature conditions.
- 774 • Previously, little was known about how buoyant calving might contribute to the
775 transformation of supraglacial lakes into full-depth lakes lacking any ice at the lake
776 bottom. Thanks to time-lapse images and photogrammetric data analysis, we were able
777 to analyse four large-scale ice-breakup events related to ice buoyancy for the period
778 September 2016 to October 2018. However, no large buoyant calving events were
779 detectable in the time-lapse images after 24.10.2018 and until (at least)
780 29.07.2020.
- 781 • Ice volumes lost by buoyant calving and by ablation through subaerial melting at the
782 lowest part of Pasterze Glacier revealed only for the period of (roughly) August 2018 to
783 August 2019 comparable values (c.1 x 10⁶ m³). In all other years, ice loss by buoyant
784 calving was substantially less important compared to subaerial ablation in terms of
785 volumetric effect. Although buoyant calving is not the most important ablation term in

786 the long term, it can result in large losses of ice and rapid geometric changes in the
787 short term. Buoyant calving can bring about a rapid transition of a lake from supraglacial
788 to full-depth and in some settings might cause a switch in the ablation regime, from
789 subaerial melt-dominated to full-depth calving dominated.

- 790 • Different ice-related processes related to hydrostatic disequilibrium have been
791 identified: limnic transgression due to ice slab lowering or tilting; drying out of
792 meltwater channels due to slab uplift or tilting of ice slabs; uplift and enlargement of
793 ice-cored terraces or icebergs; crack formation at previously stable-looking terraces;
794 sudden disintegration of ice masses into ice debris; lateral displacement or rotation of
795 icebergs; emergence of new icebergs due to buoyant calving; capsizing of icebergs;
796 detachment of ice peninsulas attached to the glacier and subsequent fragmentation into
797 several icebergs.
- 798 • Our observations suggest that buoyant calving, previously not reported from the
799 European Alps, might play an important role at alpine glaciers in the future as many
800 valley and cirque glaciers are expected to recede into valley overdeepenings or corries.

801

802 **Data availability.** ~~The data sets used in this study will be available in a data repository not~~
803 ~~specified yet.~~ Terminus position of Pasterze Glacier for the period 1998 to 2019, extent of
804 proglacial water surfaces between 1998 and 2019, and lake depth data from 13.09.2019 are
805 available in the Supplement.

806

807 Supplement. The supplement consists of three data sets and two animations: data sets: (1)
808 terminus position of Pasterze Glacier for the period 1998 to 2019, (2) extent of proglacial water
809 surfaces between 1998 and 2019, and (3) lake depth data based on echo sounding acquired on
810 13.09.2019; animations: (1) general evolution of the proglacial lake between 2010 and 2020
811 based on webcam images, and (2) ice-breakup event which occurred on the 20.09.2016. The
812 supplement related to this article is available online at: <https://doi.org/10.5194/tc-2020-227->
813 supplement.

814

815 **Author contributions.** The study was designed by AKP. Fieldwork and analysis were carried out
816 by AKP (GNSS, geophysics, bathymetry), MA (laserscanning), FB (time-lapse photography), PK
817 (land cover mapping), CZ (geophysics, bathymetry). DIB contributed to the introduction and
818 discussion. AKP prepared the manuscript with contributions from all co-authors

819

820 **Competing interests.** The authors declare that they have no conflict of interest.

821

822 **Acknowledgments.** This study was funded by different projects over the years. The most
823 important ones are: (a) Austrian Science Fund, project no. FWF P18304-N10, (b) Hohe Tauern
824 National Park authority (several projects), (c) Glockner Ökofonds (GROHAG) 2018, and (d)
825 Austrian Alpine Association (through the annual glacier monitoring program). Meteorological
826 data were kindly provided by Austrian Hydro Powers. Aerial surveys of 2018 and 2019
827 (AeroMap) were funded by project (c) and the Institute of Geography and Regional Science
828 (supported by Wolfgang Sulzer). Matthias Wecht, Gernot Seier and Wolfgang Sulzer are very

829 much thanked for supporting the aerial photograph analysis of the two AeroMap flight
830 campaigns in 2018 and 2019. Correction signals for real time kinematics ~~RTK~~-measurements
831 were kindly provided free of charge by EPOSA, Vienna. Field work was supported during
832 numerous field trips by several colleagues and numerous students especially Michael Bliem,
833 Stefan Brauchart, Alexander Dorić, Iris Hansche, Matthias Lichtenegger, Christian Lieb, Gerhard
834 Karl Lieb, Matthias Rathofer, Rupert Schwarzl, and Daniel Winkler. Melina Frießenbichler is
835 kindly acknowledged for processing TLS-data. Finally, the authors acknowledge the financial
836 support by the University of Graz.

837

838 **ORCID**

839 Andreas Kellerer-Pirklbauer <https://orcid.org/0000-0002-2745-3953>

840

841

842

843 **REFERENCES**

- 844 ~~Avian, M., Lieb, G. K., Kellerer-Pirklbauer, A., and Bauer, A.: Variations of Pasterze Glacier (Austria)~~
845 ~~between 1994 and 2006—combination of different data sets for spatial analysis, in: Proceedings of the~~
846 ~~9th International Symposium of High Mountain Remote Sensing Cartography, Graz, Austria, 14-22~~
847 ~~September 2006, 79-88, 2007.~~
- 848 Avian, M., Kellerer-Pirklbauer, A., and Lieb, G. K.: Geomorphic consequences of rapid deglaciation at
849 Pasterze Glacier, Hohe Tauern Range, Austria, between 2010 and 2013 based on repeated terrestrial
850 laser scanning data, *Geomorphology*, 310, 1-14, <https://doi.org/10.1016/j.geomorph.2018.02.003>, 2018.
- 851 Avian, M., Bauer, C., Schlögl, M., Widhalm, B., Gutjahr, K.H., Paster, M., Hauer, C., Frießenbichler, M.,
852 Neureiter, A., Weyss, G., Flödl, P., Seier, G., and Sulzer, W.: The status of earth observation techniques in
853 monitoring high mountain environments at the example of Pasterze Glacier, Austria: data, methods,
854 accuracies, processes, and scales, *Remote Sens-Basel*, 12, 1251, <https://doi.org/10.3390/rs12081251>,
855 2020.
- 856 Ballantyne, C.-K.: Paraglacial geomorphology, *Quaternary Science Reviews*, 21, 1935-2017,
857 [https://doi.org/10.1016/S0277-3791\(02\)00005-7](https://doi.org/10.1016/S0277-3791(02)00005-7), 2002.
- 858 ~~Bandini, F., Olesen, D., Jakobsen, J., Kittel, C. M. M., Wang, S., Garcia, M., and Bauer-Gottwein, P.:~~
859 ~~Technical note: Bathymetry observations of inland water bodies using a tethered single-beam sonar~~
860 ~~controlled by an unmanned aerial vehicle. *Hydrol. Earth Syst. Sci.*, 22, 4165–4181,~~
861 ~~<https://doi.org/10.5194/hess-22-4165-2018>, 2018.~~
- 862 Benn, D. I., Wiseman, S., and Hands, K. A.: Growth and drainage of supraglacial lakes on the debris-
863 mantled Ngozumpa Glacier, Khumbu Himal, Nepal, *J Glaciol*, 47, 626-638,
864 <https://doi.org/10.3189/172756501781831729>, 2001.
- 865 ~~Benn, D. I., Warren C. R., and Mottram R. H.: Calving processes and dynamics of calving glaciers, *Earth-*~~
866 ~~*Sci Rev*, 83, 143-179, <https://doi.org/10.1016/j.earscirev.2007.02.002>, 2007.~~
- 867 ~~Benn, D. I., Åström, J. A. N., Zwinger, T., Todd, J., Nick, F. M., Cook, S., Hulton, N. R., and Luckman, A.:~~
868 ~~Melt-under-cutting and buoyancy-driven calving from tidewater glaciers: new insights from discrete~~
869 ~~element and continuum model simulations, *J Glaciol*, 63, 691-702, <https://doi.org/10.1017/jog.2017.41>,~~
870 ~~2017.~~
- 871 Benn, D. I. and Evans, D. J. A.: *Glaciers and Glaciation*, 2nd edn. Hodder/Arnold Publication, London, UK,
872 2010.
- 873 ~~Bernsteiner, F.: Dynamik von Eisbruchprozessen im proglazialen See der Pasterze. Bachelor Thesis,~~
874 ~~University of Graz, Graz, 54 pp., 2019.~~

875 Bosson, J. B., Deline, P., Bodin, X., Schoeneich, P., Baron, L., Gardent, M., and Lambiel, C.: The influence
876 of ground ice distribution on geomorphic dynamics since the Little Ice Age in proglacial areas of two
877 cirque glacier systems. *Earth Surf Process Land*, 40, 666-680, <https://doi.org/10.1002/esp.3666>, 2015.

878 Boyce, E. S., Motyka, R. J., and Truffer, M.: Flotation and retreat of a lake-calving terminus, Mendenhall
879 Glacier, southeast Alaska, USA. *J Glaciol*, 53, 211-224, <https://doi.org/10.3189/172756507782202928>,
880 2007.

881 Buckel, J., Otto, J. C., Prasicek, G., and Keuschnig, M.: Glacial lakes in Austria - distribution and formation
882 since the Little Ice Age, *Global Planet Change*, 164, 39-51,
883 <https://doi.org/10.1016/j.gloplacha.2018.03.003>, 2018.

884 Buckel, J. and Otto J. C.: The Austrian Glacier Inventory GI 4 (2015) in ArcGis (shapefile) format.
885 PANGAEA, <https://doi.org/10.1594/PANGAEA.887415>, 2018.

886 Canas, D., Chan, W. M., Chiu A., Jung-Ritchie L., Leung M., Pillay L., and Waltham B.: Potential
887 environmental effects of expanding Lake Jökulsárlón in response to melting of Breiðamerkurjökull,
888 Iceland, *Cartographica*, 50, 204-213, <https://doi.org/10.3138/cart.50.3.3197G>, 2015.

889 Carrivick, J. L. and Tweed F. S.: Proglacial lakes: character, behaviour and geological importance, *Quatern*
890 *Sci Rev*, 78, 34-52, <https://doi.org/10.1016/j.quascirev.2013.07.028>, 2013.

891 Carrivick J. L. and Heckmann T.: Short-term geomorphological evolution of proglacial systems,
892 *Geomorphology*, 287, 3-28, <https://doi.org/10.1016/j.geomorph.2017.01.037>, 2017.

893 Dykes, R. C., Brook, M. S., and Winkler, S.: The contemporary retreat of Tasman Glacier, Southern Alps,
894 New Zealand, and the evolution of Tasman proglacial lake since AD 2000, *Erdkunde*, 141-154,
895 <https://doi.org/10.3112/erdkunde.2010.02.03>, 2010.

896 Gardelle, J., Arnaud, Y., and Berthier, E.: Contrasted evolution of glacial lakes along the Hindu Kush
897 Himalaya mountain range between 1990 and 2009. *Global Planet Change*, 75, 47-55,
898 <https://doi.org/10.1016/j.gloplacha.2010.10.003>, 2011.

899 Gärtner-Roer, I. and Bast, A.: (Ground) Ice in the proglacial zone: landform and sediment dynamics in
900 recently deglaciated alpine landscapes, in: *Geomorphology of proglacial systems, Geography of the*
901 *Physical Environment*, edited by Heckmann, T. and Morche D., Springer, Berlin, Heidelberg, Germany,
902 85-98, https://doi.org/10.1007/978-3-319-94184-4_6, 2019.

903 [Harris, J. and Stöcker, H.: Handbook of Mathematics and Computational Science. Springer, New York,](https://doi.org/10.1007/978-1-4612-5317-4)
904 [USA, https://doi.org/10.1007/978-1-4612-5317-4, 1998.](https://doi.org/10.1007/978-1-4612-5317-4)

905 Hirschmann, S.: Die glaziale und proglaziale Übergangszone im Bereich zweier Gletscher in den Hohen
906 Tauern, Master Thesis, University of Graz, Graz, 106 pp., ~~2017-~~[https://unipub.uni-](https://unipub.uni-graz.at/obvugr/hs/content/titleinfo/1962752)
907 [graz.at/obvugr/hs/content/titleinfo/1962752](https://unipub.uni-graz.at/obvugr/hs/content/titleinfo/1962752), 2017.

908 Holdsworth, G.: Ice calving into the proglacial Generator Lake, Baffin Island, NWT, Canada. *J Glaciol*, 12,
909 235-250, 1973.

910 Hunter L. E., and Powell R. D.: Ice foot development at temperate tidewater margins in Alaska. *Geophys*
911 *Res Let*, 25, 1923-1926, <https://doi.org/10.1029/98GL01403>, 1998.

912 Kaufmann, V., Kellerer-Pirklbauer, A., Lieb, G. K., Slupetzky, H., and Avian, M.: Glaciological studies at
913 Pasterze Glacier (Austria) based on aerial photographs 2003-2006-2009, in: *Monitoring and Modelling of*
914 *Global Changes: A Geomatics Perspective*, edited by: Yang, X. and Li, J., Springer, Berlin, Heidelberg,
915 Germany, 173-198, https://doi.org/10.1007/978-94-017-9813-6_9, 2015.

916 Kellerer-Pirklbauer, A.: The supraglacial debris system at the Pasterze Glacier, Austria: spatial
917 distribution, characteristics and transport of debris, *Z. Geomorph. N.F.* 52, Suppl., 1, 3-25,
918 <https://doi.org/10.1127/0372-8854/2008/0052S1-0003>, 2008.

919 Kellerer-Pirklbauer, A. and Kulmer, B.: The evolution of brittle and ductile structures at the surface of a
920 partly debris-covered, rapidly thinning and slowly moving glacier in 1998–2012 (Pasterze Glacier,
921 Austria), *Earth Surf Processes*, 44, 1034–1049. <https://doi.org/10.1002/esp.4552>, 2019.

922 Kellerer-Pirklbauer, A., Lieb, G. K., Avian, M., and Gspurning, J.: The response of partially debris-covered
923 valley glaciers to climate change: The Example of the Pasterze Glacier (Austria) in the period 1964 to
924 2006, *Geogr Ann A*, 90 A/4, 269-285, <https://doi.org/10.1111/j.1468-0459.2008.00345.x>, 2008.

925 Kellerer-Pirklbauer, A., Avian, M., Hirschmann, S., Lieb, G. K., Seier, G., Sulzer, W., and Wakonigg, H.:
926 Sudden disintegration of ice in the glacial-proglacial transition zone of the largest glacier in Austria, EGU
927 General Assembly, Vienna, Austria, 23–28 April 2017, EGU2017-12069, 2017.

928 King, O., Dehecq, A., Quincey, D., and Carrivick, J.: Contrasting geometric and dynamic evolution of lake
929 and land-terminating glaciers in the central Himalaya. *Global Planet Change*, 167, 46-60,
930 <https://doi.org/10.1016/j.gloplacha.2018.05.006>, 2018.

931 King, O., Bhattacharya, A., Bhambri, R., and Bolch, T.: Glacial lakes exacerbate Himalayan glacier mass
932 loss, *Sci Rep*, 9, 18145, <https://doi.org/10.1038/s41598-019-53733-x>, 2019.

933 Kirkbride, M. P. and Warren, C. R.: Tasman Glacier, New Zealand: 20th-century thinning and predicted
934 calving retreat, *Global Planet Change*, 22, 11-28, [https://doi.org/10.1016/S0921-8181\(99\)00021-1](https://doi.org/10.1016/S0921-8181(99)00021-1), 1999.

935 Kneisel, C. and Käab, A.: Mountain permafrost dynamics within a recently exposed glacier forefield
936 inferred by a combined geomorphological, geophysical and photogrammetrical approach. *Earth Surf*
937 *Proc Land*, 32, 1797–1810, <https://doi.org/10.1002/esp.1488>, 2007.

938 Kneisel, C. and Hauck, C.: Electrical methods, in: *Applied Geophysics in Periglacial Environments*, edited
939 by: Hauck, C. and Kneisel, C., Cambridge University Press, Cambridge, UK, 3-27,
940 <https://doi.org/10.1017/CBO9780511535628>, 2008.

- 941 Krisch, P. and Kellerer-Pirklbauer, A.: Landschaftsdynamik im glazialen-proglazialen Übergangsbereich
942 der Pasterze im Zeitraum 1998-2015, *Carinthia II*, 209./129, 565-580, 2019.
- 943 Lieb, G. K., and Kellerer-Pirklbauer, A.: Die Pasterze, Österreichs größter Gletscher und seine lange
944 Messreihe in einer Ära massiven Gletscherschwundes, in: *Gletscher im Wandel - 125 Jahre*
945 *Gletschermessdienst des Alpenvereins*, edited by: Fischer, A., Patzelt, G., AchRAINER, M., Groß, G., Lieb,
946 G. K., Kellerer-Pirklbauer, A., and Bandler, G., Springer, Heidelberg, Germany, 31-51,
947 <https://doi.org/10.1007/978-3-662-55540-8>, 2018.
- 948 Liu, Q., Mayer, C., Wang, X., Nie, Y., Wu, K., Wei, J., and Liu, S.: Interannual flow dynamics driven by
949 frontal retreat of a lake-terminating glacier in the Chinese Central Himalaya. *Earth Planet Sc Lett*, 546,
950 116450, <https://doi.org/10.1016/j.epsl.2020.116450>, 2020.
- 951 ~~Loke, M.H.: *Electrical imaging surveys for environmental and engineering studies—a practical guide to*
952 *2-D and 3-D surveys*, Penang, Malaysia, 2000.~~
- 953 ~~Loke, M. H. and Barker, R.D.: Rapid least-squares inversion of apparent resistivity pseudosections using a
954 quasi-Newton method. *Geophys Prospect*, 44, 131-152. [https://doi.org/10.1111/j.1365-](https://doi.org/10.1111/j.1365-2478.1996.tb00142.x)
955 [2478.1996.tb00142.x](https://doi.org/10.1111/j.1365-2478.1996.tb00142.x), 1996.~~
- 956 Otto, J. C.: Proglacial Lakes in High Mountain Environments, in: *Geomorphology of proglacial systems,*
957 *Geography of the Physical Environment*, edited by Heckmann, T. and Morche D., Springer, Berlin,
958 Heidelberg, Germany, 231-247, https://doi.org/10.1007/978-3-319-94184-4_14, 2019.
- 959 Pant, S. R. and Reynolds J. M.: Application of electrical imaging techniques for the investigation of
960 natural dams: an example from the Thulagi Glacier Lake, Nepal. *J Nepal Geolog Soc*, 22, 211-218, 2000.
- 961 Richardson, S. D. and Reynolds, J. M.: An overview of glacial hazards in the Himalayas, *Quatern Int*,
962 65/66, 31-47, [https://doi.org/10.1016/S1040-6182\(99\)00035-X](https://doi.org/10.1016/S1040-6182(99)00035-X), 2000.
- 963 Röhl, K.: Thermo-erosional notch development at fresh-water-calving Tasman Glacier, New Zealand. *J*
964 *Glaciol*, 52, 203-213, <https://doi.org/10.3189/172756506781828773>, 2009.
- 965 Seier, G., Kellerer-Pirklbauer, A., Wecht, W., Hirschmann, S., Kaufmann, V., Lieb, G. K., and Sulzer, W.:
966 UAS-based change detection of the glacial and proglacial transition zone at Pasterze Glacier, Austria,
967 *Remote Sens-Basel*, 9, 549, 1-19, <https://doi.org/10.3390/rs9060549>, 2017.
- 968 Schomacker, A.: Expansion of ice-marginal lakes at the Vatnajökull ice cap, Iceland, from 1999 to 2009.
969 *Geomorphology*, 119, 232-236, <https://doi.org/10.1016/j.geomorph.2010.03.022>, 2010.
- 970 Schomacker, A. and Kjær, K. H.: Quantification of dead-ice melting in ice-cored moraines at the high-
971 Arctic glacier Holmströmbreen, Svalbard, *Boreas*, 37, 211-225, [https://doi.org/10.1111/j.1502-](https://doi.org/10.1111/j.1502-3885.2007.00014.x)
972 [3885.2007.00014.x](https://doi.org/10.1111/j.1502-3885.2007.00014.x), 2008.

973 Stokes, C.R., Popovnin, V., Aleynikov, A., Gurney, S.D., Shahgedanova, M.: Recent glacier retreat in the
974 Caucasus Mountains, Russia, and associated increase in supraglacial debris cover and supra-/proglacial
975 lake development. *A Glaciol*, 46, 195-203, <https://doi.org/10.3189/172756407782871468>, 2007.

976 [Wagner, T.J., James, T.D., Murray, T. and Vella, D.: On the role of buoyant flexure in glacier calving.](https://doi.org/10.1002/2015GL067247)
977 [Geophys Res Lett](https://doi.org/10.1002/2015GL067247), 43, 232-240, <https://doi.org/10.1002/2015GL067247>, 2016.

978 ~~Wakonigg, H., and Lieb, G.K.: Die Pasterze und ihre Erforschung im Rahmen der Gletschermessungen,~~
979 ~~Kärntner Nationalpark-Schriften, 8, Großkirchheim, 99-115, 1996.~~

980 Warren, C., Benn, D. I., Winchester V., and Harrison, S.: Buoyancy-driven lacustrine calving, Glaciar Nef,
981 Chilean Patagonia, *J Glaciol*, 47, 135-146, <https://doi.org/10.3189/172756501781832403>, 2001.

982 Zuo Z. and Oerlemans J.: Numerical modelling of the historic front variation and the future behaviour of
983 the Pasterze Glacier, Austria. *Ann Glaciol*, 24, 234-241, <https://doi.org/10.3189/S0260305500012234>,
984 1997.

985

986

987 **Tables and table captions**

988

989 **Table 1:** Technical parameters of aerial surveys between 1998 and 2019 used in this study. For

990 2003, 2006, and 2009 see also Kaufmann et al. (2015). KAGIS = GIS Service of the Regional

991 Government of Carinthia; BEV = Federal Office of Metrology and Surveying.

Aerial survey	Acquisition date	Source	Geometric resolution of calculated orthophotos
1998	Aug. 1998	National Park Hohe Tauern	0.5 m
2003	13.08.2003	Kaufmann et al. (2015)	0.5 m
2006	22.09.2006	Kaufmann et al. (2015)	0.5 m
2009	24.08.2009	Kaufmann et al. (2015)	0.5 m
2012	18.08.2012	KAGIS / BEV	0.2 m
2015	11.07.2015	KAGIS / BEV	0.2 m
2018	11.09.2018	KAGIS / BEV	0.2 m
2018	15.11.2018	AeroMap GmbH	0.1 m
2019	21.09.2019	AeroMap GmbH	0.09 m

992

993

994

995

996 **Table 2: Affected ice masses during the three ice-breakup events IB2 (09.08.2018), IB3**
 997 **(26.09.2018), and IB4 (24.10.2018). For approach see text. Number in italics are not considered**
 998 **for the total volume calculation. Lateral displacement of icebergs is not considered.**

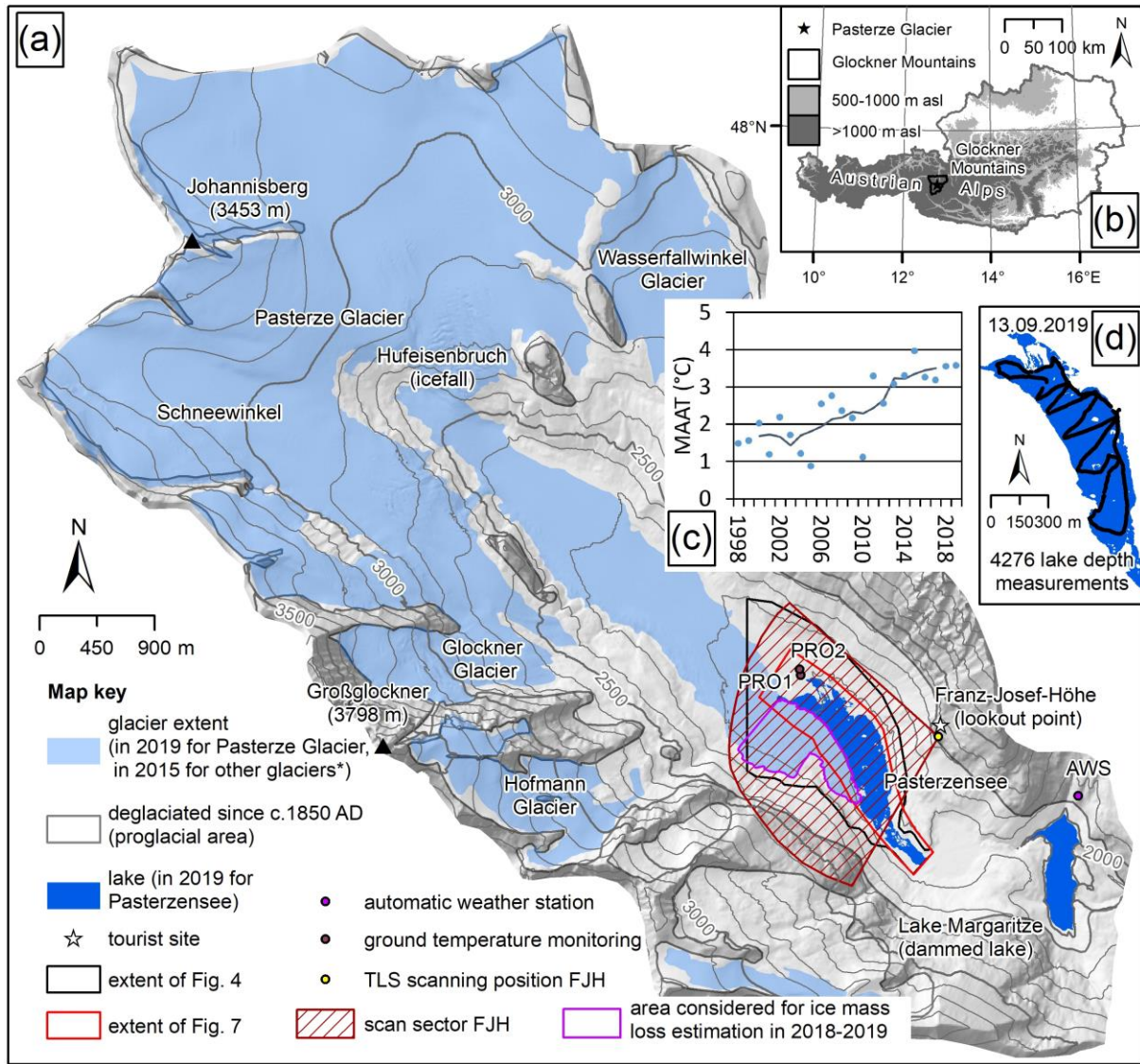
999

<u>Event</u>	<u>Process</u>	<u>State</u>	<u>Volume above water level / 10% (m³)</u>	<u>Total volume / 100% (m³)</u>
<u>IBE2</u>	<u>ice peninsula detachment</u>	<u>before detachment</u>	<u>3206.8</u>	<u>32,068</u>
	<u>ice emergence</u>	<u>after emergence</u>	<u>2364.8</u>	<u>23,648</u>
<u>IBE3</u>	<u>ice emergence</u>	<u>after emergence</u>	<u>3216.9</u>	<u>32,169</u>
	<u>Ice uplift</u>	<u>before uplift</u>	<u>7060.3</u>	<u>70,603</u>
		<u>after uplift</u>	<u>48,369.2</u>	<u>483,692</u>
		<u>difference</u>	<u>41,308.9</u>	<u>413,089*</u>
<u>IBE4</u>	<u>ice peninsula detachment</u>	<u>before detachment</u>	<u>2833.6</u>	<u>28,336</u>
	<u>ice disintegration</u>	<u>after emergence</u>	<u>50,926.8</u>	<u>509,268</u>
<u>Sum</u>				<u>1,038,578</u>

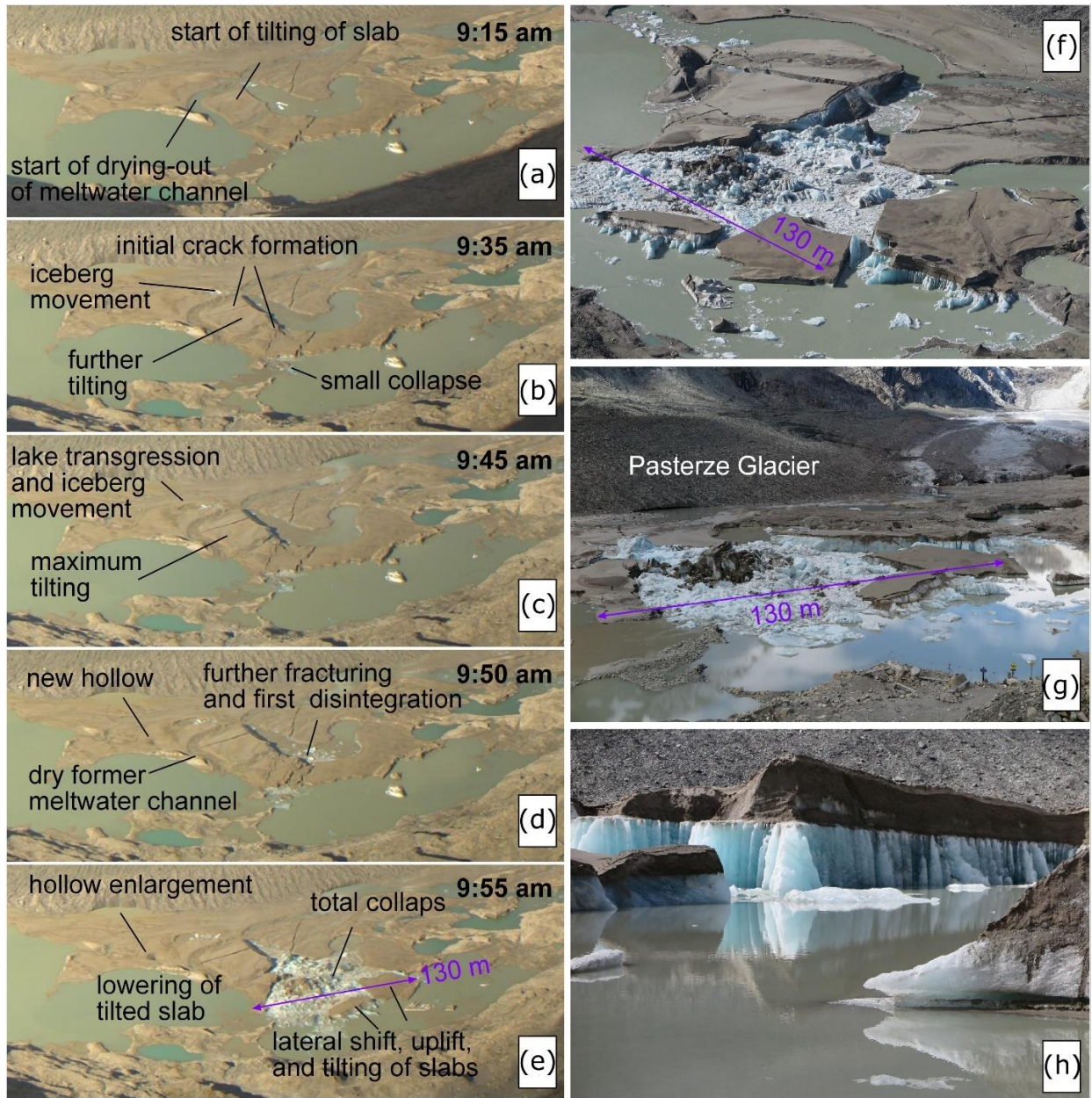
1000 (* difference considered in the total)

1001

1002



1004
 1005 **Figure 1:** Pasterze Glacier. (a) Location of Pasterze Glacier at the foot of Großglockner (3798m asl).
 1006 Relevant sites are indicated; (b) location of the study area within Austria; (c) mean annual air
 1007 temperature (MAAT) at the automatic weather station (AWS) Margaritze in 1998-2019 (single years and
 1008 5-year running mean); (d) position of 4276 lake depth measurements carried out on 13.09.2019.
 1009 Hillshade in the background of (a) from 2012 source KAGIS. Extent of glacier and lake in 2019 this study.
 1010 Glacier extent of 2015 (*) based on Buckel and Otto (2018). Glacier extent of c.1850 based on own
 1011 mapping.



1012

1013 **Figure 2:** Evolution of the proglacial area at Pasterze Glacier during a period of only 40 minutes

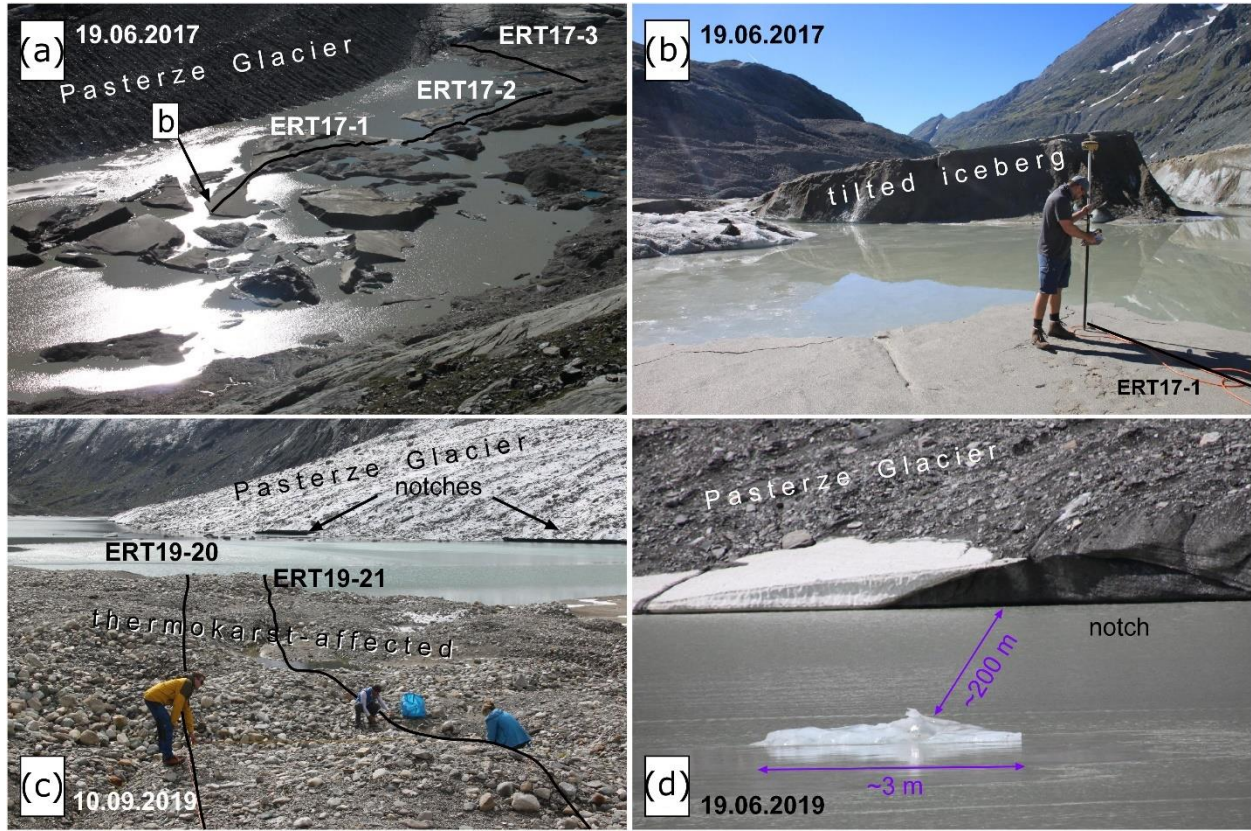
1014 (20.09.2016; from 9:15 to 9:55 a.m.) due to loss of hydrostatic disequilibrium and buoyancy as depicted

1015 by an automatic time-lapse camera (a-e) and observed in the field a few hours after the event (f-h). Note

1016 the sudden fracturing between 9:50 and 9:55 am. (a-e) provided by GROHAG, (f-h) provided by Konrad

1017 Mariacher, 20.09.2016.

1018



1020

1021

Figure 3: Field impressions of the ice-contact lake and its close surrounding: (a) overview image

1022

depicting the distribution of water bodies, icebergs and debris-covered dead-ice bodies on 19.06.2017.

1023

Courses of ERT profiles presented in Figure 9 are shown; (b) starting point of ERT17-1 surveyed by

1024

DGPSGNSS; (c) thermokarst-affected area with courses of two ERT profiles on 10.09.2019. Note the

1025

Pasterze Glacier and thermo-erosional notches at the lake level; (d) buoyant calving of a small iceberg

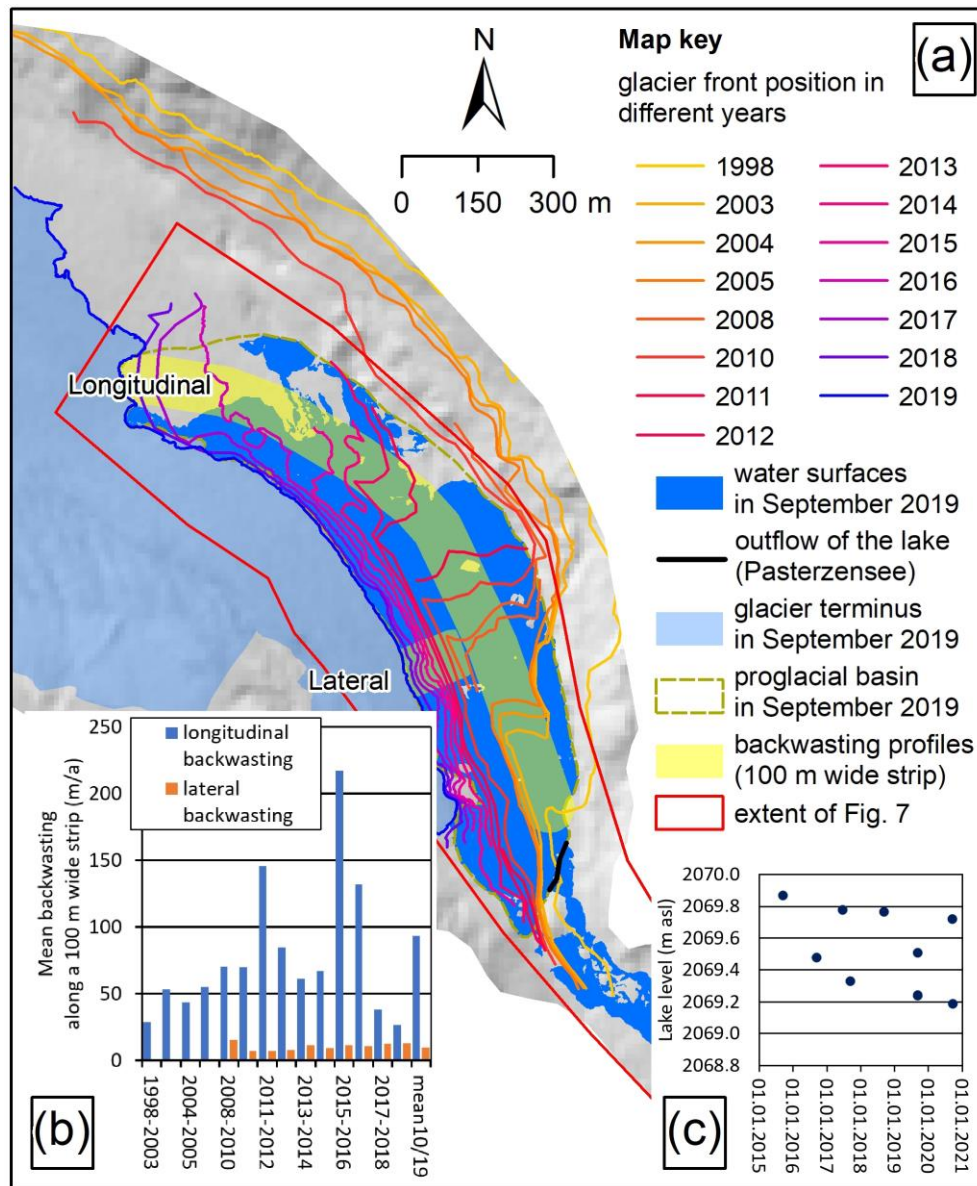
1026

←(“shooter”) c.200 m from the subaerial glacier front observed during fieldwork (all photographs

1027

Andreas Kellerer-Pirklbauer).

1028



1029

1030

1031

1032

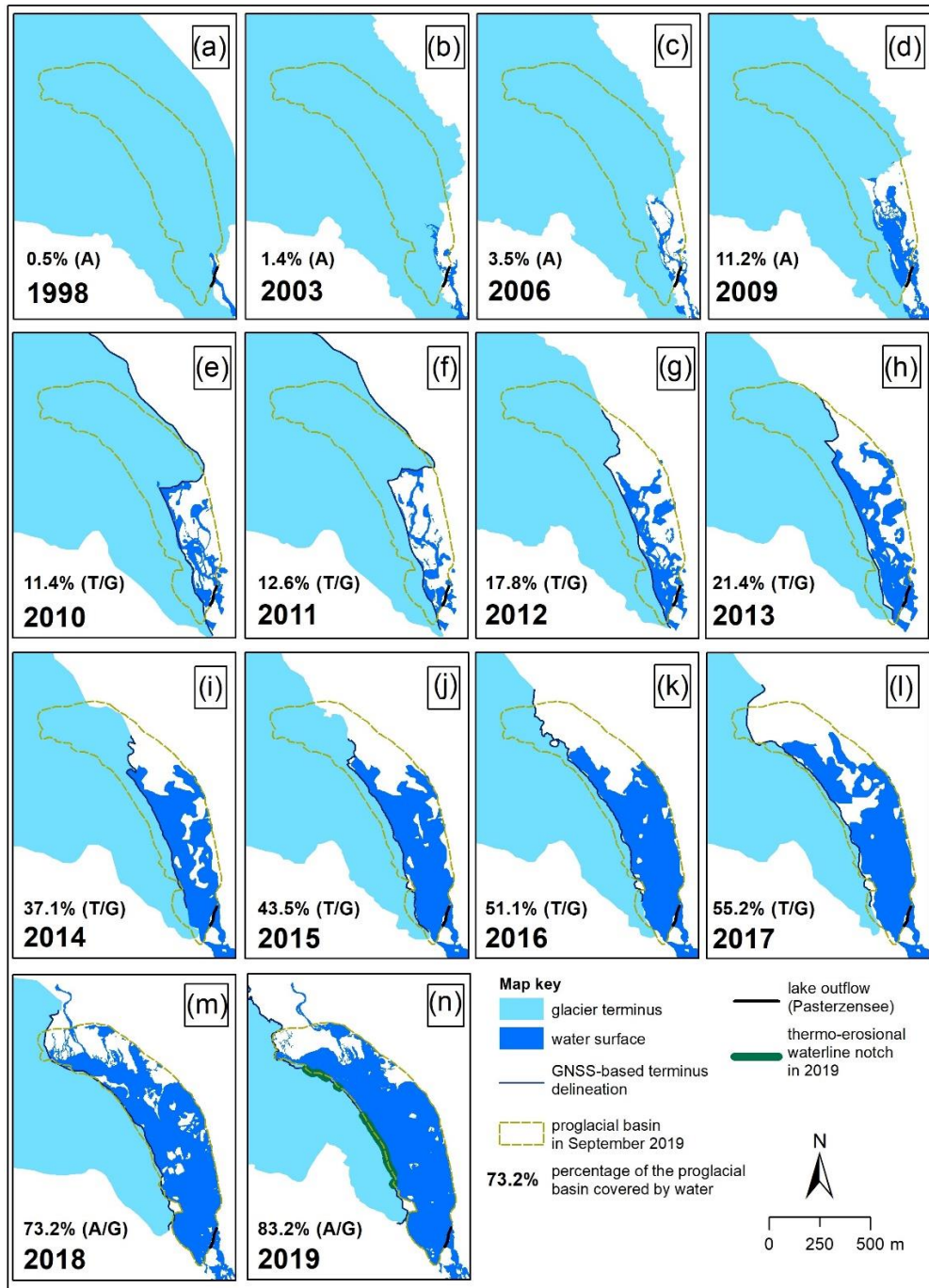
1033

1034

1035

1036

Figure 4: Terminus position of Pasterze Glacier for the period 1998 to 2019 DGPS-GNSS data and lake-level variability of Lake Pasterzensee in the period 2015 to 2020 derived mainly from sequential GNSS data. (a) the extent of water surfaces including the Lake Pasterzensee and the delineation of the proglacial basin is shown for September 2019. 100 m wide profiles (lateral and longitudinal) used for backwasting calculations are indicated. Backwasting results are depicted in (b) (background hillshade based on 10m DTM, KAGIS). (c) lake level elevations for nine stages between 17.09.2015-22.09.2020 (all between 11 am and 3 pm).



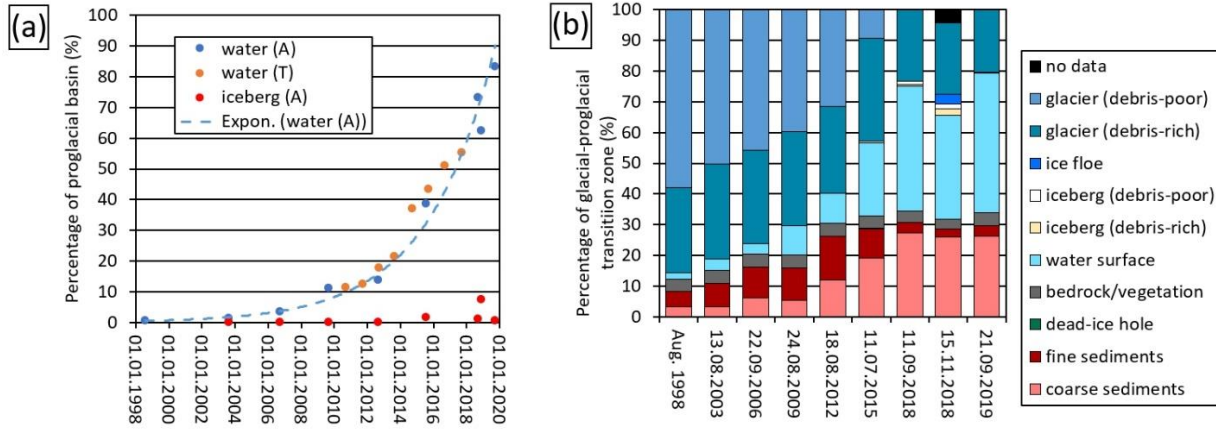
1037

1038 **Figure 5:** Glacier recession and evolution of proglacial water surfaces since 1998 at Pasterze Glacier. The

1039 proglacial basin as defined for September 2019 is depicted in all maps for comparison. For data sources

1040 refer to text and Table 1. A=airborne photogrammetry, T=terrestrial laserscanning, ~~DG~~=~~DGPS~~GNSS.

1041



1042

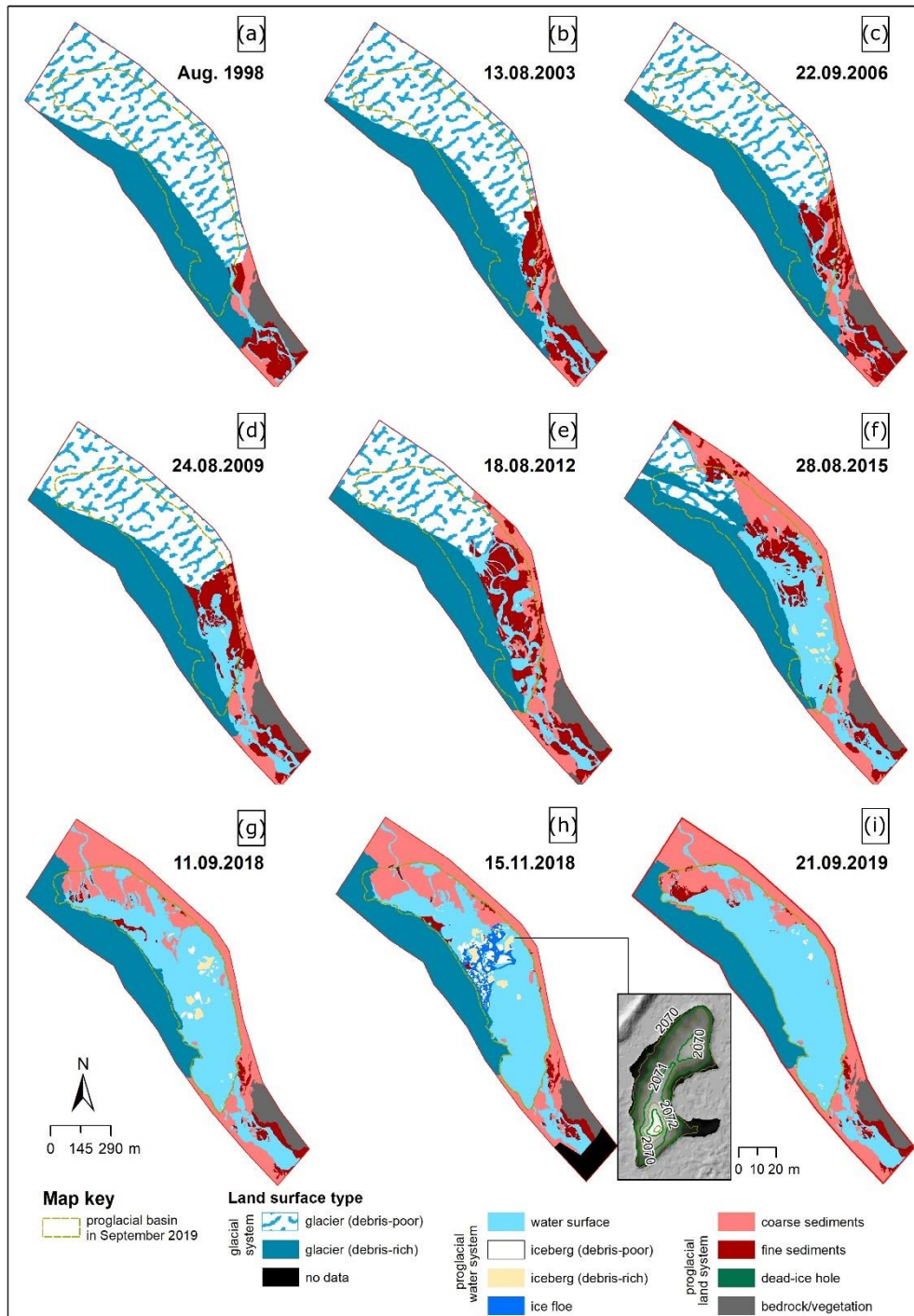
1043 **Figure 6:** Glacial-proglacial transition zone: (a) Evolution of water surfaces and icebergs in the proglacial
 1044 basin (100%=0.37 km²; Fig. 5 for delineation) of Pasterze Glacier since 1998 based on airborne
 1045 photogrammetry/A or terrestrial laserscanning/T data. Icebergs only based on airborne
 1046 photogrammetry/A; (b) summarising graph depicting relative changes of different surface types in the
 1047 glacial-proglacial zone (100%=0.76 km²; extent as shown in Fig. 7) since 1998.

1048

1049

1050

1051



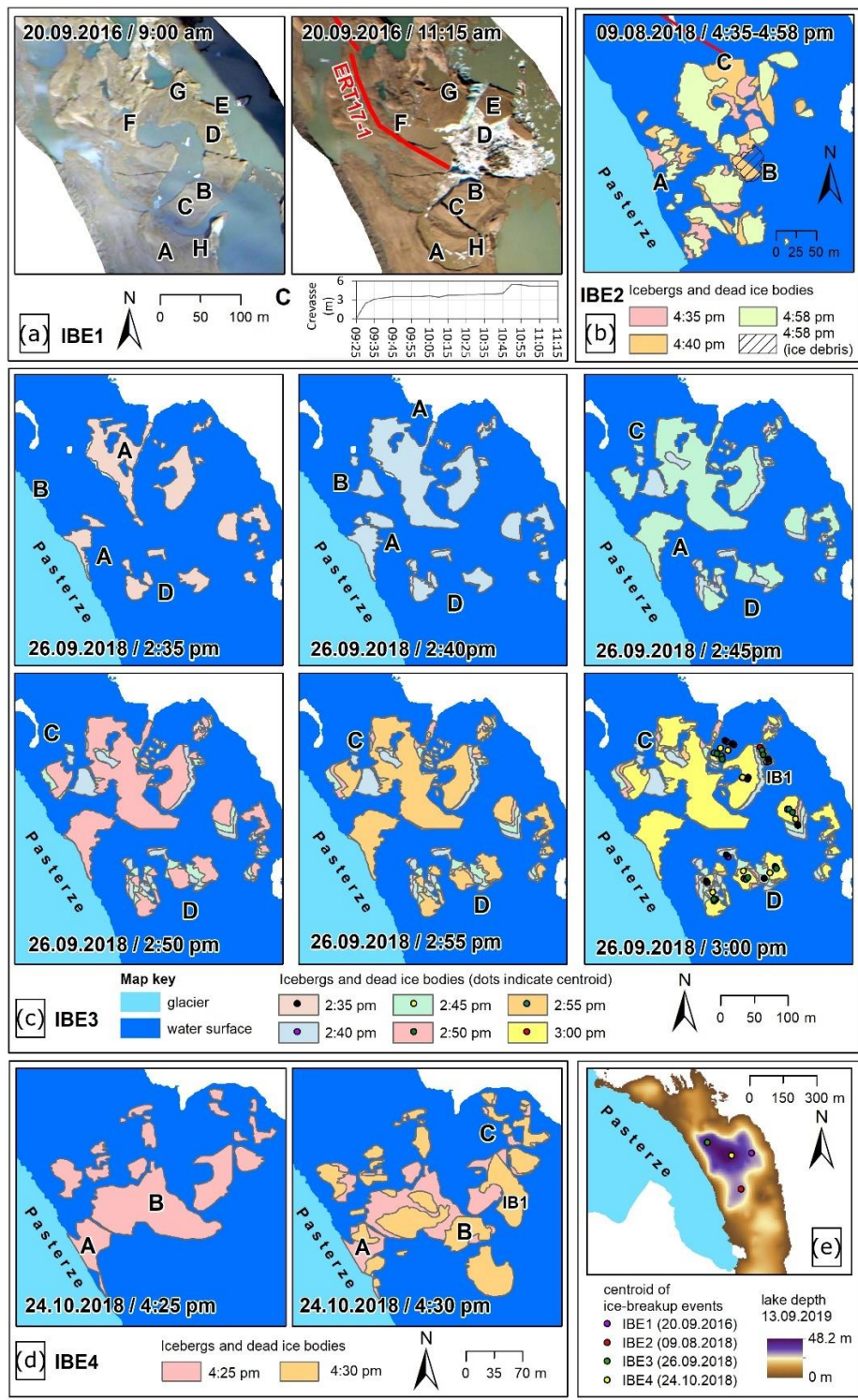
1052

1053 **Figure 7:** Land cover evolution in the glacial-proglacial transition zone (0.76 km²) of Pasterze Glacier

1054 between 1998 and 2019 based on visual landform classification. The proglacial basin as defined for

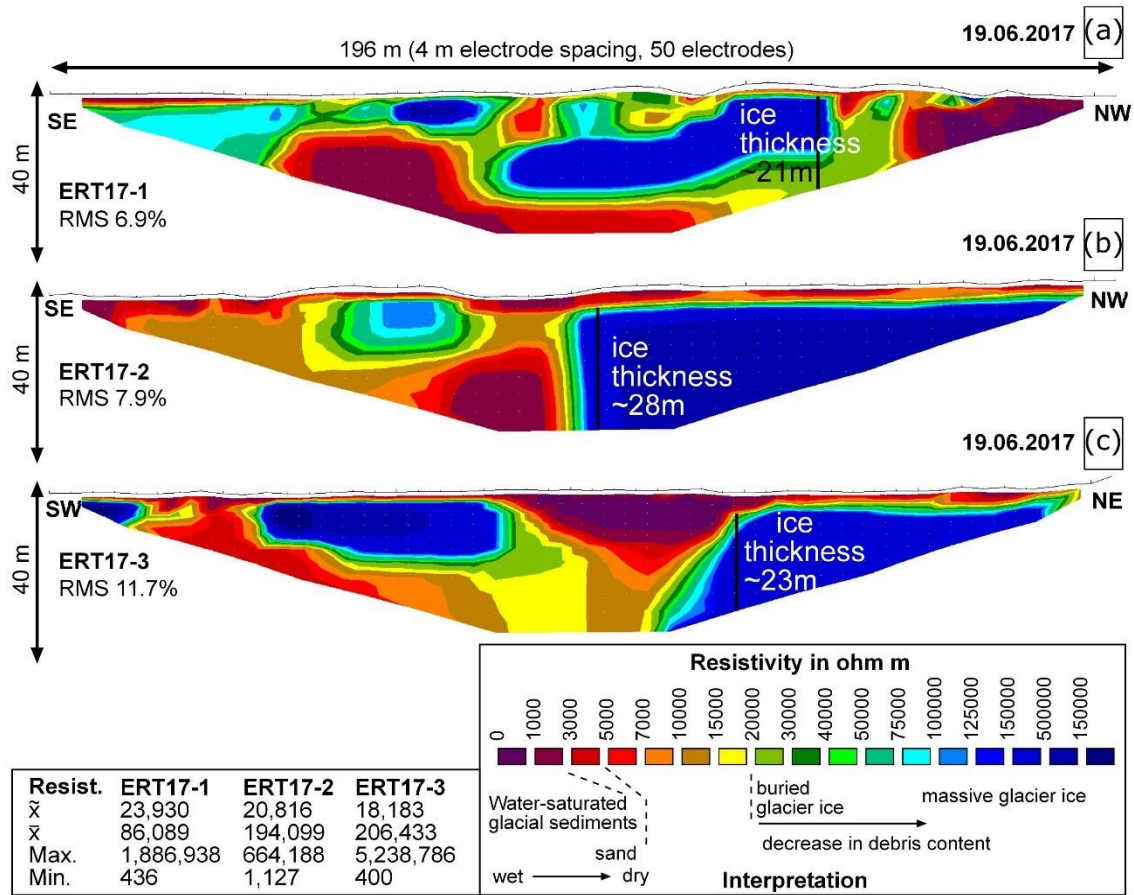
1055 September 2019 is depicted in all maps for comparison. For data sources refer to text and Table 1.

1056 Inset map in (h) depicts a digital elevation model and contour lines (0.5 m interval) of iceberg IB1.



1057
 1058 **Figure 8:** Ice-breakup events (IBE) at the ice-contact lake Pasterzensee monitored by time-lapse
 1059 photography: (a) IBE1 20.09.2016; (b) IBE2 09.08.2018; (c) IBE3 26.09.2018; (d) IBE 4 24.10.2018; (e)
 1060 overview map of the events. Capital letter in the maps indicate different processes (for details see text).

1061



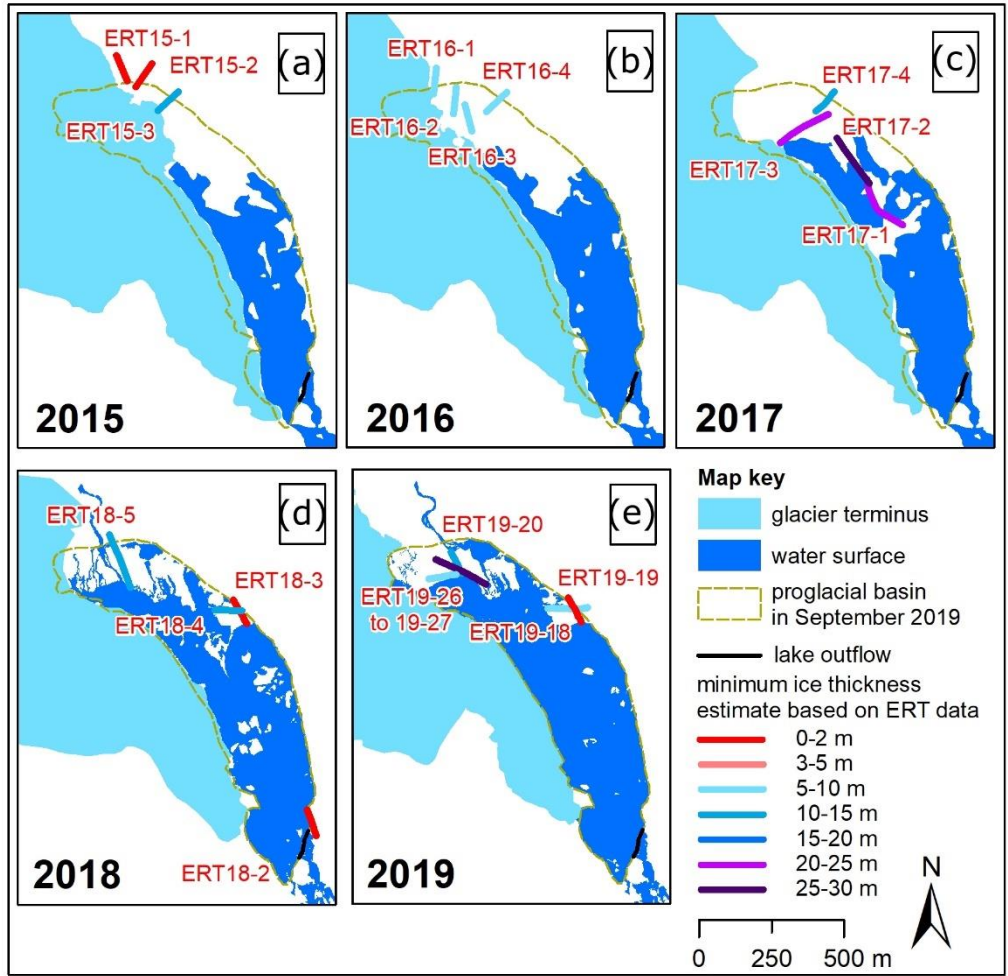
1062

1063 **Figure 9:** ERT results (Wenner array) and interpretation of three profiles (50 electrodes, 4 m spacing,
 1064 length 196 m) measured in the proglacial area of Pasterze Glacier on 19.06.2017 (location: Figs 3, 10).
 1065 Summary statistics in the inset table: (a) ERT17-1 – ice lens with a thickness of c.21 m; (b) ERT17-2 –ice
 1066 thickness c.28m; (c) ERT17-3 –ice thickness c.23m. For (b) and (c) - ice thickness exceeded the depth of
 1067 ERT penetration.

1068

1069

1070



1072

1073

Figure 10: Interpreted minimum ice thicknesses based on electrical resistivity tomography (ERT) data

1074

(for estimation approach see Fig. 9) in the proglacial area of Pasterze Glacier for (a) 30.09.2015, (b)

1075

13.09.2016, (c) 19.06.2017, (d) 13.09.2018, and (e) 09.09.2019 as well as 10.09.2019. “Minimum”

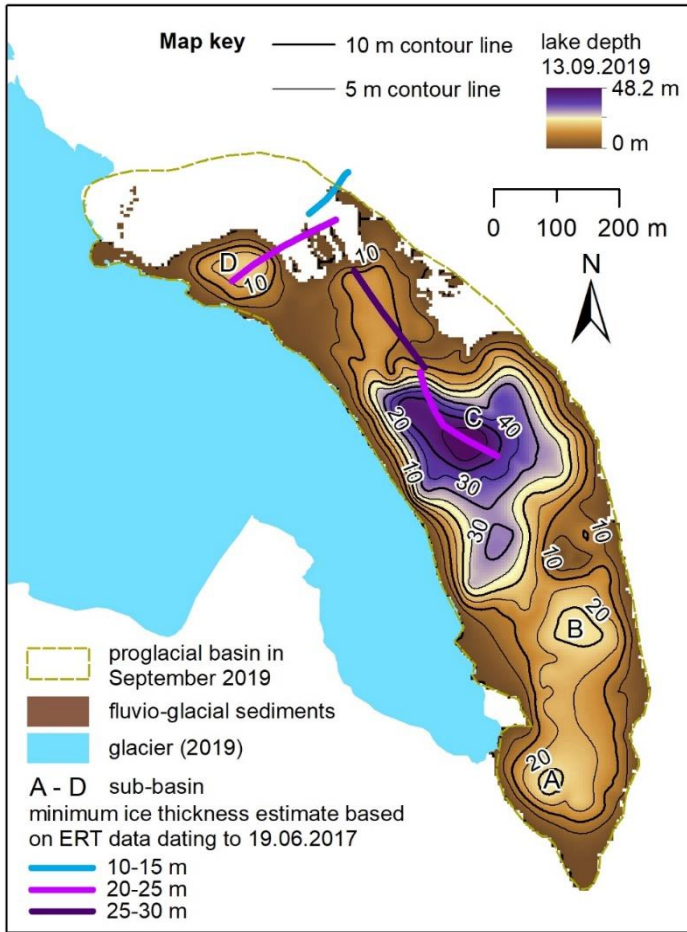
1076

means in this case that the base of the ice core was commonly below the depth of ERT penetration.

1077

1078

1079

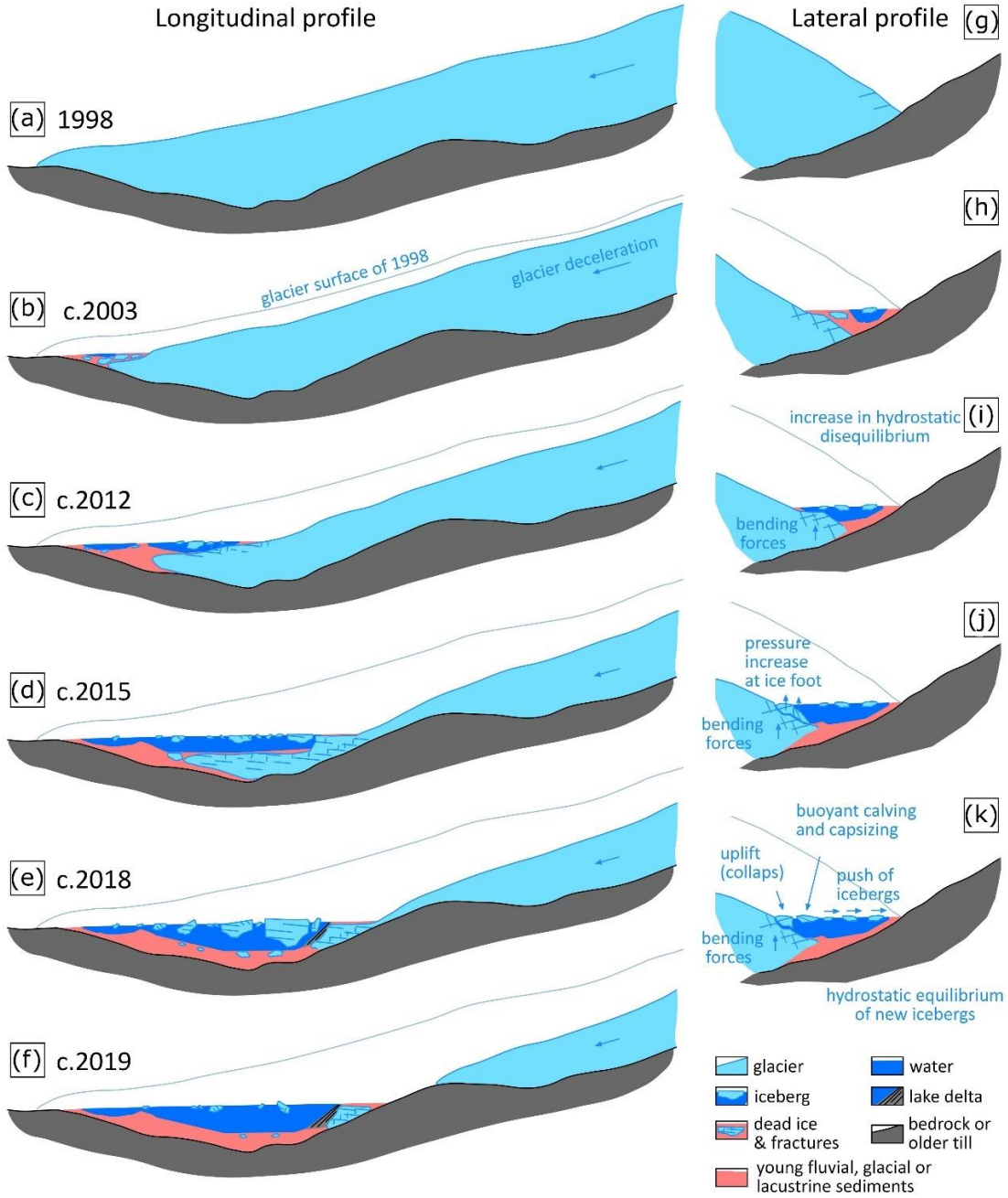


1080

1081 **Figure 11:** Lake bathymetry based on echo sounding data acquired in 2019 and its relationship to the
1082 ERT data from 2017: glacier extent and lake bathymetry in September 2019 (5 m grid resolution); the
1083 extent of the proglacial basin as defined for September 2019 is drawn in the map for orientation.

1084

1085



1087

1088 **Figure 12:** Conceptual model of the evolution of the glacial-proglacial transition zone at Pasterze Glacier
 1089 since 1998 behind a bedrock threshold: panels (a) to (f) depict changes along a longitudinal profile at the
 1090 east side (supraglacial debris-poor) of the glacier tongue; panels (g) to (k) visualize lateral changes and
 1091 related processes.